

The 2QDES Pilot : The luminosity & redshift dependence of quasar clustering

Ben Chehade^{1*}, T. Shanks¹, J. Findlay^{1,4}, N. Metcalfe¹, U. Sawangwit¹, M. Irwin², E. González-Solares², S. Fine⁸, M. J. Drinkwater³, S. Croom^{6,7}, R. J. Jurek⁹, D. Parkinson⁵, R. Bielby¹

¹*Centre for Extragalactic Astronomy, Department of Physics, Durham University, South Road, Durham DH1 3LE, U.K.*

²*Institute of Astronomy, Univ. of Cambridge, Madingley Road, Cambridge, CB3 0HA, UK*

³*School of Mathematics and Physics, University of Queensland, Brisbane, QLD 4072, Australia*

⁴*Department of Physics & Astronomy, University of Wyoming, 1000 E. University, Department 3905, Laramie, WY 82071, USA*

⁵*School of Mathematics and Physics, University of Queensland, Brisbane, Queensland 4072, Australia*

⁶*Sydney Institute for Astronomy (SfA), School of Physics, University of Sydney, NSW 2006, Australia*

⁷*ARC Centre of Excellence for All-sky Astrophysics (CAASTRO)*

⁸*Department of Physics, University of Western Cape, Bellville 7535, Cape Town, South Africa*

⁹*CSIRO Astronomy and Space Science, Australia Telescope National Facility, PO Box 76, Epping, NSW 1710, Australia*

17 March 2016

ABSTRACT

We present a new redshift survey, the 2dF Quasar Dark Energy Survey pilot (2QDESp), which consists of ≈ 10000 quasars from ≈ 150 deg² of the southern sky, based on VST-ATLAS imaging and 2dF/AAOmega spectroscopy. Combining our optical photometry with the WISE (W1,W2) bands we can select essentially contamination free quasar samples with $0.8 < z < 2.5$ and $g < 20.5$. At fainter magnitudes, optical UVX selection is still required to reach our $g \approx 22.5$ limit. Using both these techniques we observed quasar redshifts at sky densities up to 90 deg⁻². By comparing 2QDESp with other surveys (SDSS, 2QZ and 2SLAQ) we find that quasar clustering is approximately luminosity independent, with results for all four surveys consistent with a correlation scale of $r_0 = 6.1 \pm 0.1 h^{-1}$ Mpc, despite their decade range in luminosity. We find a significant redshift dependence of clustering, particularly when BOSS data with $r_0 = 7.3 \pm 0.1 h^{-1}$ Mpc are included at $z \approx 2.4$. All quasars remain consistent with having a single host halo mass of $\approx 2 \pm 1 \times 10^{12} h^{-1} M_\odot$. This result implies that either quasars do not radiate at a fixed fraction of the Eddington luminosity or AGN black hole and dark matter halo masses are weakly correlated. No significant evidence is found to support fainter, X-ray selected quasars at low redshift having larger halo masses as predicted by the ‘hot halo’ mode AGN model of Fanidakis et al. (2013). Finally, although the combined quasar sample reaches an effective volume as large as that of the original SDSS LRG sample, we do not detect the BAO feature in these data.

Key words: L^AT_EX 2_ε - catalogues - quasars:general - galaxies:active - galaxies:Seyfert

1 INTRODUCTION

Quasars are a very luminous subset of the active galactic nuclei (AGN) population. Due to their high intrinsic luminosities they can be exploited in a wide variety of cosmological and astrophysical studies. Quasars possess an ultraviolet excess (UVX) of emission with respect to stars. The UVX property has previously been exploited by large area surveys to perform quasar selection, such as 2QZ (Smith et al. 2005), 2SLAQ (Richards et al. 2005) and SDSS (Richards et al. 2002). In addition to their UVX property, quasars

possess an excess of emission with respect to stars in the infrared. This method of selecting quasars is sometimes known as the KX (K-band excess) technique and has also been used to photometrically select quasars (see Maddox et al. 2012). The aim of the 2QDESp survey is to maximise the measured sky density of quasars between $0.8 < z < 2.5$ and hence minimise the correlation function errors for both cosmological and quasar physics studies.

The 2QZ (Croom et al. 2005, hereafter C05), 2SLAQ (da Ângela et al. 2008, hereafter dA08) and SDSS (Ross et al. 2009, hereafter R09) surveys all measured the quasar correlation function in approximately the same redshift interval ($0.8 < z < 2.5$). As each of the surveys had different magnitude limits but similar redshift distributions we can compare these directly to one another to mea-

* E-mail: ben.chehade@durham.ac.uk

sure the luminosity dependence of quasar clustering. Shanks et al. (2011, hereafter S11) discuss the implications of these three surveys measuring a consistent value of r_0 , the clustering scale. Of particular interest to galaxy formation models is the apparent independence (S11; dA08, and Shen et al. 2009) of quasar clustering with luminosity. S11 examines the results from optical clustering measurements (C05; dA08; R09) and attempts to reconcile these results in context of existing models and finds no evidence for strong luminosity dependence of quasar clustering. This is surprising given the measured relation between optical luminosity and black hole mass, M_{BH} , (Peterson et al. 2004) and black hole mass and dark matter halo mass, M_{Halo} , (Ferrarese 2002; Fine et al. 2006).

However, Fanidakis et al. (2013) predict that less luminous quasars inhabit higher mass halos and reported that X-ray selected quasars inhabit higher mass halos ($\sim 10^{13} M_{\odot}$) than found in optical studies ($\sim 10^{12} M_{\odot}$). If optically and X-ray selected quasars sample distinct populations there may be no contradiction to the conclusions of S11. We aim to measure ~ 80 quasars deg^{-2} , comparable to the sky density quasars in deep X-ray surveys (Allevato et al. 2011). At these space densities the significant overlap between X-ray and optical quasar samples should result in larger correlation lengths if X-ray selected quasars inhabit higher mass halos.

Here we describe the first quasar survey (2QDESp) using VLT survey telescope (VST)-ATLAS (Shanks et al. 2015) optical photometry with follow-up spectroscopic observations made using 17 nights of AAT time using 2dF and the AAOmega spectrograph. Combining 2QDESp with several previous quasar surveys we measure the luminosity dependence of quasar clustering for the combined sample. In Section 2 we describe the imaging data and quasar selection techniques. In Section 5 we describe our spectroscopic follow-up of targets and the resulting quasar catalogue. In Section 6 we discuss the methods used to measure quasar clustering and the results from the 2QDESp sample before incorporating the other surveys into our analysis. From this combined sample we make measurements of the luminosity and redshift dependence of quasar clustering in Sections 6.3 and 6.4. We discuss our results and their implications in Section 7. We assume $H_0 = 100 h \text{ km s}^{-1} \text{ Mpc}^{-1}$ and a flat cosmology from Planck Collaboration et al. (2014) with $\Omega_M = 0.307$. *ugriz* magnitudes are quoted in the AB magnitude system unless stated otherwise, WISE magnitudes are left in their native Vega system.

2 IMAGING

2.1 Imaging

2.1.1 VST-ATLAS

The VLT Survey Telescope (VST) is a 2.6 m wide-field survey telescope with a $1^\circ \times 1^\circ$ field of view and hosts the OmegaCAM instrument. OmegaCAM (Kuijken et al. 2004) is an arrangement of 32 CCDs with $2k \times 4k$ pixels, resulting in $16k \times 16k$ image with a pixel scale of $0.21''$. The VST-ATLAS is an ongoing photometric survey that will image $\approx 4700 \text{ deg}^2$ of the southern extragalactic sky with coverage in *ugriz* bands. The survey takes two sub-exposures (exposure time varies across filters) per 1 degree field with a 25×85 arcsecond dither in X and Y to ensure coverage across interchip gaps. The sub-exposures are then processed and stacked by the Cambridge Astronomy Survey Unit (CASU). The CASU pipeline outputs catalogues that are cut at approximately 5σ and provides fixed aperture fluxes and morphological classifications of detected objects. The *u*-band catalogue comprises ‘forced

photometry’ at the position of *g*-band detections; no other band is forced. The processing pipeline and resulting data products are described in detail by Shanks et al. (2015). Bandmerged catalogues were produced using TOPCAT and STILTS software (Taylor 2005, 2006). Unless otherwise stated, for stellar photometry we use a $1''$ radius aperture (*aper3* in the CASU nomenclature). ATLAS photometry is calibrated using nightly observations of standard stars. The calibration between nights can vary by ± 0.05 mag (see Shanks et al. 2015 for details). We performed a further calibration on the fields we observed prior to target selection to ensure agreement between VST-ATLAS fields and the SDSS stellar locus, as described in Section 4.0.6. With the VST-ATLAS survey under halfway complete during our spectroscopy, the selection of 2dF pointing positions was governed by the progress of ATLAS. The fields are not generally distributed over a spatially contiguous region, although their seeing and magnitude limits are representative of the survey as a whole. The morphological star-galaxy classification we use is that supplied as default in the CASU catalogues. This classification is discussed in detail by González-Solares et al. (2008). We test the morphological completeness for different colour-colour selections in Section 4.0.3.

2.1.2 WISE

The NASA satellite Wide-field Infrared Survey Explorer (WISE) (Wright et al. 2010), mapped the entire night sky in four passbands between $3.4 - 22 \mu\text{m}$. The survey depth varies over the sky but approximate 5σ limits for point sources are $W1 = 16.83$ and $W2 = 15.60$ mag. in the Vega system. The W1 and W2 bands have point spread functions (PSFs) of $6.1''$ and $6.4''$ respectively compared with $\approx 1''$ in the VST-ATLAS bands. A comparison¹ between WISE catalogue positions and the USNO CCD Astrograph Catalog (UCAC3) catalogue shows that even at the faintest limits of W1 there is $< 0.5''$ rms offset between the two catalogues. We matched ATLAS optical photometry to the publicly available WISE All-Sky Source Catalogue using a $1''$ matching radius. Given the size of the WISE PSF we examine the possibility of WISE-ATLAS mismatching. For sky density of WISE sources at $|b| > 30^\circ$ we calculate that 1 in 25 quasars identified in WISE will have a blended WISE source within $3''$. Compared to this value, the contribution from quasar-quasar pairs will be smaller. Given the other advantages of using WISE selection, we view this effect as essentially negligible.

3 OTHER QUASAR REDSHIFT SURVEYS

Here we introduce three additional quasar surveys that were used to measure the clustering of optically selected quasars. To aid comparison between these surveys and our own we summarise the method of quasar selection for each survey, the measured space density, area and size. In Section 6 we remeasure the correlation function for these surveys, verifying our measurement against previously published values (see Table 3). We then combine these survey with the 2QDESp sample to better constrain the autocorrelation function.

3.1 2QZ

The 2QZ survey (Croom et al. 2004) covers approximately 750 deg^2 of the sky in two contiguous areas of equal size. The quasar

¹ <http://wise2.ipac.caltech.edu/docs/release/allsky/expsup/sec2.2.html>

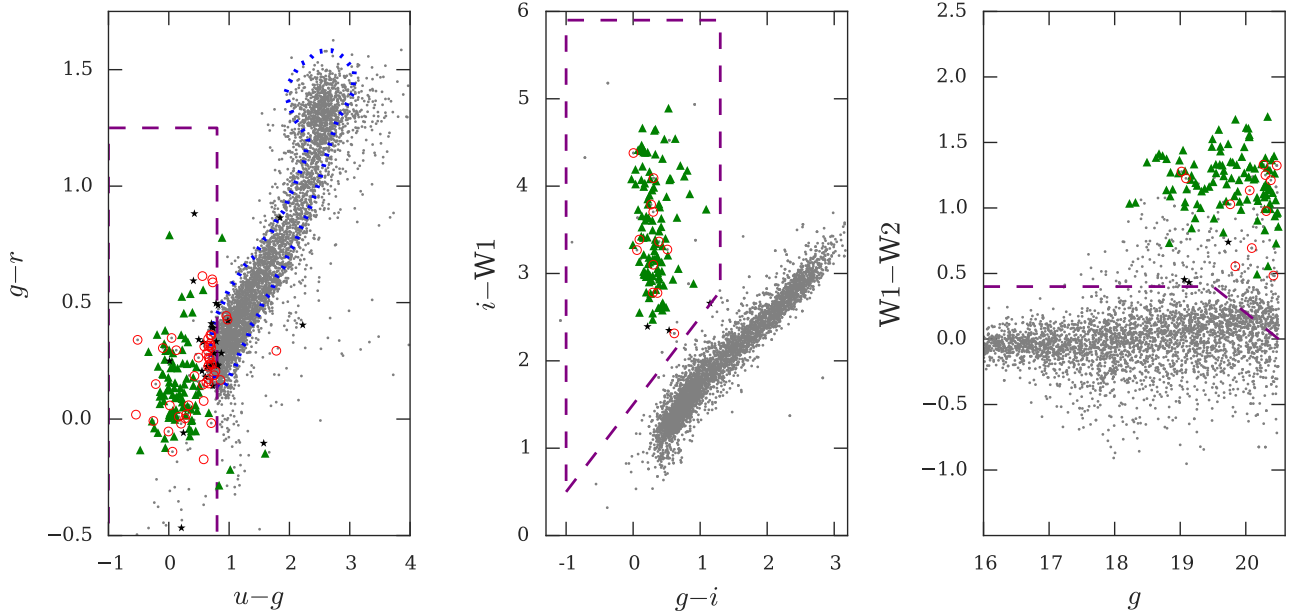


Figure 1. In the left panel we show the ugr colour space of the field centred at $23^h16^m - 26^d01^m$. We show all objects identified in the g -band as point-sources (between $16 \leq g \leq 20.5$) as grey dots. We show the SDSS Stripe 82 stellar locus (dotted blue line) and our ugr colour cuts (purple dashed lines) from Section 4.0.4. Spectroscopically confirmed quasars within our target redshift range ($0.8 < z < 2.5$) are shown as green triangles and confirmed stars are shown as black five-point stars. Sources without a positive identification are outlined with a red circle. In the middle panel we show the same objects in the $giW1$ colour space and in the right panel we show the $gW1W2$ colour space.

sample consists of over 22500 spectroscopically confirmed sources at redshifts less than 3.5 and apparent magnitudes $18.25 < b_J < 20.85$. Quasars are selected based on their broadband optical colours from automated plate measurement (APM) scans from United Kingdom Schmidt Telescope (UKST) photographic plates. Colour selection is performed using $u - b_J$ vs. $b_J - r$. The measured quasar density is ≈ 30 quasars deg^{-2} .

3.2 SDSS DR5

The SDSS DR5 uniform sample (Schneider et al. 2007) contains 30000 spectroscopically confirmed quasars between redshifts $0.3 \leq z \leq 2.2$ and an apparent magnitude limit of $i_{SDSS} \leq 19.1$ over $\approx 4000 \text{ deg}^2$. This sample was selected using single epoch photometry from the SDSS using the algorithm given in Richards et al. (2002). The sample is described in detail by R09 and has a measured quasar density of ≈ 8 quasars deg^{-2} .

3.3 2SLAQ

The 2SLAQ survey (Croom et al. 2009) overlaps two subregions within the 2QZ survey area, with an average quasar density ≈ 45 quasars deg^{-2} and redshifts of $z \leq 3$. The 2SLAQ survey is based on SDSS photometry and measures redshifts for quasars of apparent magnitudes $20.5 < g_{SDSS} < 21.85$. This sample was designed to be used in conjunction with the observations from the 2QZ survey, (see dA08).

4 2QDESP QUASAR SELECTIONS

4.0.1 Quasar density $g \leq 22.5$

Previously, 2QZ measured a completeness corrected sky density of 30 quasars deg^{-2} at $b_J < 20.85$. 2SLAQ reached a nominal density of 45 deg^{-2} at $20.5 < g_{SDSS} < 21.85$. dA08 combined the 2QZ and 2SLAQ samples to produce a higher density sample of $\approx 80 \text{ deg}^{-2}$. However, the high incompleteness of 2SLAQ meant this high density was only achieved after the application of completeness corrections. In this survey we aim to measure 80–100 quasars deg^{-2} in the redshift range $0.8 < z < 2.5$ in ~ 1 hour 2dF exposures; we demonstrate the feasibility of our aims below.

4.0.2 Quasar Luminosity Function

The first concern of the 2QDES pilot is whether or not the luminosity function of quasars predicted 80+ quasars deg^{-2} within our targeted redshift ($0.8 < z < 2.5$) and magnitude ($16 < g < 22.5$) range. A small number of quasar redshift surveys have explored this redshift range to fainter limits than 2SLAQ although always in relatively small areas. Fine et al. (2012) made a survey based on Pan-STARRS Medium Deep Survey imaging. As well as using colour selection, Fine et al. (2012) also used variability from many epochs of imaging to select their quasar candidates. To a magnitude limit of $g = 22.5$ their measured quasar density was $88 \pm 6 \text{ deg}^{-2}$ ($0.8 < z < 2.5$).

In SDSS Stripe 82 Palanque-Delabrouille et al. (2013) covered $\approx 15 \text{ deg}^2$ and measured a completeness corrected quasar density of 99 ± 4 quasars deg^{-2} . This was to the same depth as 2QDESP ($g \leq 22.5$) and in a narrower redshift range ($1 \leq z \leq 2.2$). However,

both these authors relied on multi-epoch photometry reaching 50% completeness for point sources at $g = 24.6$ (c.f. $g \sim 23$ for VST-ATLAS).

Finally, spectroscopic follow-up of X-ray sources in the XMM-COSMOS field (Brusa et al. 2010) has measured a quasar density of 110 quasars deg^{-2} within our redshift interval to a depth of $g < 22.5$ ($i \lesssim 22.2$).

Thus from these comparisons to other surveys we can be confident that there exist a sufficiently high space density of quasars within the $g \leq 22.5$ limit of the survey. However, these complete samples are often selected from deeper imaging with the added benefit of selecting quasars from their variability.

4.0.3 Photometric incompleteness from VST-ATLAS

The second question we address is whether the VST-ATLAS catalogues are of sufficient depth to select 80–100 quasars deg^{-2} . As an approximate test of our photometric completeness we rely on the u and g -bands where quasars have the colour $u-g < 0.5$. In the g -band the limit $g < 22.5$ which is ~ 0.7 mag brighter than the median 5σ depth of VST-ATLAS as such we assume we are always complete in this band. The 5σ limits are based on sky noise but as the u -band is forced this limit may not provide a good estimate of the image depth. We match to the deeper KIDS survey (de Jong et al. 2013) in an area of VST-ATLAS with $u_{5\sigma} = 21.7$ (90% of tiles have fainter limits, see Shanks et al. 2015). We find that the use of forced photometry in the u results in 50% completeness (c.f. KIDS) at $u=22$ which is 0.3 mag deeper than the 5σ limit. Applying the limits $g < 22.5$ and $u < 22$ (with $0.8 < z < 2.5$) to the Fine et al. (2012) data we recover 80 ± 6 quasars deg^{-2} . Assuming median depth limits ($u = 21.99$) gives 87 ± 6 quasars deg^{-2} .

The number counts of the Fine et al. suggest the sample is complete to $g \approx 21.9$. This incompleteness at fainter magnitudes will lower the estimated return of quasars in the VST-ATLAS data. We note that the more complete data of Palanque-Delabrouille et al. (2013) returns $\sim 10\%$ more quasars than Fine et al. (2012).

We have taken a conservative approximation of our photometry and a conservative estimate of the true quasar density and found the VST-ATLAS photometry is sufficiently deep to return our minimum target density (80 quasars deg^{-2}). By assuming more representative photometry and comparing to a more complete quasar sample we expect these estimated densities to increase. We finally note that in the 2QDESp survey (see Sections 5.2 and Table A) that 90% of 2dF pointings have a $u_{5\sigma} > 21.85$ i.e. the u imaging is slightly better than found in VST-ATLAS as a whole.

4.0.4 $ugri$ selection

The UVX property of quasars was successfully used by both 2QZ and SDSS to select quasars in our target redshift range ($0.8 < z < 2.5$). As our photometric bands are the same as those used by SDSS, we can base our colour selection on work from the SDSS collaboration. We used known 2QZ quasars within the ATLAS footprint to determine the colour cuts suitable for use with VST-ATLAS aperture photometry.

For reference, we show the location of our cuts in ugr colour space in the left panel of Figure 1. Our selection criteria were as follows;

- $-1 \leq (u - g) \leq +0.8$
- $-1.25 \leq (g - r) \leq 1.25$
- $(r - i) \geq 0.38 - (g - r)$

We applied this colour selection in a 2dF field with typical VST-ATLAS depth and seeing and found ≈ 600 candidates deg^{-2} , where we considered only point sources (in the g -band) and targets between $16 < g < 22.5$. These cuts selected a large area in colour space (minimising the effect of colour incompleteness) and therefore resulted in a high sky density of targets but with significant stellar contamination. We relied on the combination of these cuts and the XDQSO algorithm (see Section 4.0.6) to minimise this stellar contamination, particularly for fainter targets $21.5 < g < 22.5$.

Due to the proximity of the quasar locus to main sequence (MS) stars, photometric errors are a concern for optical quasar selection. Galaxies may be incorrectly identified as point-sources from their morphology but galaxy colours are sufficiently non-quasar like that galaxy contamination is not considered to be problematic. Morphological incompleteness may be introduced, however, by identifying point-sources as extended sources and therefore not selecting them as quasar candidates. To mitigate this effect we rely on the deeper VST-ATLAS bands to perform our morphological cuts (the g and r -bands). We relied on two bands to account for the possibility of poor image quality affecting the morphological classification in a single band.

4.0.5 Optical and mid-IR selection

By combining the mid-infrared photometry from WISE with the optical bands from VST-ATLAS we achieve a larger separation between the stellar locus and our target quasars than is possible using optical colours alone (see Figure 1). Unlike the $ugri$ colours this selection relies on the infrared excess of emission to differentiate between stars and quasars.

Quasars in our target redshift range have a mean $g-W1 = 4$ with a large dispersion $\approx \pm 1$. The 5σ limits are $g \approx 23.25$ and $W1 \approx 16.83$. As such the depth of our mid-IR selection is limited by the depth of the WISE photometry.

In the centre panel of Figure 1 we show the $g-i$ colour plotted against the $i-W1$ colour. The stellar locus is clearly identifiable. The right hand panel shows the mid-IR colour $W1-W2$ as a function of g band magnitude. The latter colour selection helped to remove any remaining stellar contamination that was left by the $g-i : i-W1$ colour cut.

The colour cuts we applied are given here;

- $(i-W1) \geq (g-i) + 1.5$
- $-1 \leq (g-i) \leq 1.3$
- $(i-W1) \leq 8$
- $(W1-W2) > 0.4 \ \& \ g < 19.5$
- $(W1-W2) > -0.4g + 8.2 \ \& \ g > 19.5$

Within a typical 2dF pointing, this target selection returns ≈ 100 candidates deg^{-2} . This algorithm therefore supplies optimal target density to observe all candidates on the 2dF in a single exposure. However, to meet our target density we required this algorithm to be both highly complete and free from contamination. We used the $giW1$ colours to test our morphological classification of sources from their g -band imaging, by separating the galaxy and stellar loci in colour space. We determined that of the stars identified by their colour, $91.5 \pm 0.5\%$ were identified as point sources by the g -band morphological classification. We tested the morphological classification in the r -band with the $rzW1$ colours and found a similar value.

4.0.6 XDQSO Algorithm

Automated quasar selection algorithms typically compare broadband colours to model quasar colours (or some library of previously observed quasars). As the VST-ATLAS survey has the same filter set as the SDSS survey, there exists a legacy of quasar selection code (such as Richards et al. 2004; Kirkpatrick et al. 2011; Bovy et al. 2011). Bovy et al. (2011) demonstrated the success of the XDQSO² algorithm and we applied this algorithm throughout our observing program. The XDQSO algorithm takes as input the colours of a source and compares this to empirical observations of quasars and stars. The code outputs a relative likelihood (PQSO $\in [0, 1]$) that an object is either a star or a quasar. The XDQSO algorithm uses SDSS as its training data and so we must consider both colour terms between SDSS and VST-ATLAS filters and differences in photometric zeropoints. If these differences between SDSS and VST-ATLAS are small then we shall be able to implement the XDQSO algorithm without modification. At the time of our spectroscopic programme, VST-ATLAS photometry was supplied in the Vega system. To convert to the SDSS system we adjusted the zeropoints of the individual VST-ATLAS tiles to get good agreement with the SDSS Stripe 82 coadd photometry for stars. In the left panel of Figure 1 we show the outline of the stellar locus from Stripe 82; the VST-ATLAS photometry is seen to be in good agreement with this deeper photometry. We refer the reader to Shanks et al. (2015) where the SDSS-VST colour terms are shown to be small.

The output of this selection algorithm is continuous and assigns candidates with a relative quasar likelihood. As such, we are not limited by a lack of candidates but by the availability of instrument fibres. Whilst the precise sky density of XDQSO candidates varies with image quality (and hence sky position), selecting candidates ranked according to their PQSO value limits us to observing candidates with PQSO ≥ 0.7 .

5 SPECTROSCOPIC OBSERVATIONS

5.1 2dF & AAOMEGA

Spectroscopic observations were made with the 2dF-AAOMega instrument on the AAT. The 2dF is a fibre positioning system for the AAOMega multi-object spectrograph which is capable of simultaneously observing 392 objects over ≈ 3.14 deg² field of view. Fibres are positioned by a robotic arm and are fed to the spectrograph. The 2dF also implements a tumbling system that allows for a second plate to be configured whilst the first is being observed. AAOMega is a dual beam spectrograph that utilises a red/blue dichroic beam splitter, splitting the light at 5700Å. The observations were made using the 580V and 385R gratings for the blue and red arms of the spectrograph respectively. The gratings have resolving power of $R=1300$ and central wavelengths of 4800Å and 7250Å for the blue and red arms. The useful wavelength range in our configuration is 3700Å to 8800Å.

We made no nightly observations of standard stars so our spectra do not have an accurate absolute calibration. The 2DFDR³ data reduction pipeline combines the spectra from the red and blue arms of the spectrograph. To achieve this, the spectra are calibrated to a common scale with an arbitrary normalisation due to unknown

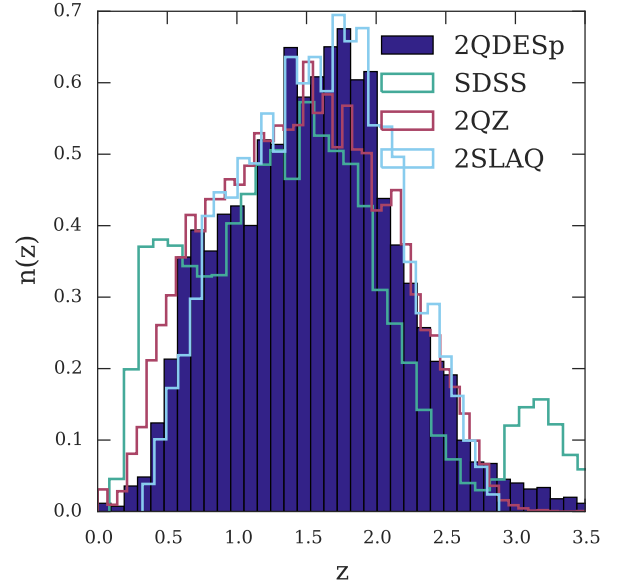


Figure 2. We show the redshift distribution of the 2QDESp spectroscopic quasar sample as the shaded region. For comparison we include the redshift distributions for the SDSS DR5, 2SLAQ and 2QZ samples.

aperture losses, via a transfer function derived from previous observations of the standard star EG 21.

Of the 392 2dF fibres (not including 8 for guide stars) 20 fibres for sky subtraction. The remaining ≈ 372 fibres were used for science targets. The fibre allocation software CONFIGURE⁴ (v7.17) allows input targets to have priorities associated with them. The observing priorities allow the software to make a decision about the importance of placing fibres. This allowed us to prioritise our spectroscopic targets according to their likelihood of being a quasar. This prioritisation was one of the requirements of the target selection process.

Exposure times varied between 0.7 – 2 hours to account for observing conditions. All our data was reduced using the 2DFDR pipeline (v5.35) using default parameters. We measured quasar redshifts of the spectra with the RUNZ programme (Saunders et al. 2004).

5.2 Resulting QSO catalogue

We developed a combination of the three techniques described in Section 4 to optimise our quasar selection over the duration of the pilot survey. We divided the selection into two major implementations. The first (chronological) selection relied solely on the optical photometry from VST-ATLAS in the form of *ugri* and XDQSO. Later implementation of the selection algorithm applied these techniques in conjunction with optical-IR colour cuts. We label these algorithms in Table A as “*ugriXDQSO*” and “*ugriXDQSO1W2*” respectively.

The “*ugriXDQSO*” target selection was based on *ugri* colours with the XDQSO algorithm used to rank those targets. The “*ugriXDQSO1W2*” selection algorithm gave candidates meeting

² v0.6

³ <http://www.aao.gov.au/science/software/2dfdr>

⁴ <http://www.aao.gov.au/science/software/configure>

the optical+IR conditions from Section 4.0.5 the highest priority, with remaining candidates prioritised based primarily on their PQSO.

In Table A we present the results of our spectroscopic observations. We list the field locations and the dates of our observations, the number of quasars identified in a given pointing, exposure times, mean spectral signal-to-noise and a guide to the target selection used.

As variation in spectral signal-to-noise affects our measured quasar density, we look to parametrise our different fields in a meaningful manner so that we can compare the effectiveness of our selection algorithms. To account for varying spectroscopic incompleteness between different observations we compare the number of bright $g \leq 20.5$ quasars between our fields (see column “ $N_{QSO \leq 20.5}$ ” in Table A). At these brighter magnitudes we are approximately spectroscopically complete for quasars. We show in Table A the faint limit in the g -band that contains 90% of our spectroscopically confirmed quasar sample and see that we are suitably bright to be photometrically complete in the $ugriz$ bands.

Having accounted for spectroscopic incompleteness we expect variation in our measured quasar density to be primarily determined by our selection algorithm and the number of background stars (see Section 5.5). Whilst the VST-ATLAS is limited to high galactic latitudes we note that the number of stars in a 2dF pointing can vary significantly (see Table A). We include in Table A the number of point sources of magnitude $g \leq 21.5$ under the heading N_{stars} and see this density vary by up to a factor of three. This variation is primarily determined by galactic latitude (c.f. $\approx 5\%$ from zeropoint errors).

Our spectroscopic programme was awarded 17 nights of observing time to develop a QSO selection algorithm as preparation for a larger programme. We obtained redshifts for $\approx 10\,000$ quasars with apparent magnitudes $g \leq 22.5$ and $1.55 < z < 2.5$ (80% of the sample lies within $0.8 < z < 2.5$). We present the redshift distribution of our quasars in Figure 2 and include the redshift distributions for 2QZ, 2SLAQ and SDSS for comparison. We see that the SDSS $n(z)$ has a second peak at $z \approx 3.1$ which is due to a secondary colour selection designed to identify quasars at this redshift. When comparing between surveys we limit to $0.3 < z < 2.9$ and so ensure good agreement between the redshift distributions.

5.2.1 Redshift errors

Here we consider factors which affect the measurement of quasar redshifts. Poor quality spectra will cause errors in redshift estimation as well as incompleteness due to failure to identify the target as a quasar. Reliance on a small number of quasar emission lines will also cause systematic errors due to mis-identification of emission features, as noted by Croom et al. (2004). We have a number of repeat observations that we can use to quantify the redshift error. The RUNZ code allows for three quality flags $qop = 5, 4$ or 3 for reliable redshifts.

Restricting our analysis to the highest quality spectra ($qop = 5$) we find a redshift error of $\sigma(z)/z = 0.002$, comparing repeat observations as in Croom et al. (2004). This corresponds to $\sim 600 \text{ km s}^{-1}$ or $\sim 2h^{-1} \text{ Mpc}$ (comoving) at our mean redshift. We next compare the highest quality to the intermediate quality ($qop = 4$) spectra. We take any difference in redshift greater than $\Delta z = 0.01$ as a redshift failure. Intermediate quality spectra have a redshift failure rate of $6 \pm 2\%$ and an error of $\sigma(z)/z = 0.002$, excluding $\Delta z > 0.01$. Similarly we find $\sigma(z)/z = 0.002$ for our lowest quality spectra ($qop = 3$) but this time with a failure rate of $16 \pm 12\%$.

We quantify the rate of redshift failure due to line mis-identification. Having examined quasars with repeat observations we find that redshift failures occur for $9 \pm 1\%$ of quasars, over all redshifts, magnitudes and spectral quality.

5.3 Effectiveness of Quasar selection methods

We introduced the optical-IR colour cuts in Section 4.0.5; we review their effectiveness here and compare to the XDQSO technique which relies on UVX techniques to identify quasars. To compare these selection techniques we examine one of the most complete fields ($23^h 16^m - 26^d 01^m$) where we find over 80 quasars deg^{-2} between $0.8 < z < 2.5$ and $16 < g < 22.5$.

In Figure 1 we show the distribution of our quasar sample in the ugr , $giW1$ and $gW1W2$ colour spaces. We include only point sources with $g < 20.5$. As noted in section 4.0.5 the left and middle panels of Figure 1 show a difference in distance between the quasars and the stellar locus. At fainter magnitudes ($g > 20.5$) the photometric scatter will become larger and so that the effective separation between the stars (mainly type A and F) and quasars will be reduced. The increased distance from the stellar locus seen in $giW1$ (compared to the distance in ugr colour space) suggests that this selection may suffer from less stellar contamination than using ugr photometry and that any stellar contamination might come from different spectral types of stars.

We examine the apparent purity of the $giW1W2$ colour selection by comparing its effectiveness against the XDQSO algorithm. We are limited in the $giW1W2$ selection by the depth of the WISE photometry and so must take this into account when comparing to the XDQSO algorithm. We limit our comparison to $g < 20.5$ and treat photometric and spectroscopic incompleteness for quasars as negligible. In Table 1 we take all $giW1W2$ quasar candidates with $g < 20.5$ and find that 3% of these sources are stars, based on spectroscopic observations. If we assume all of the non-identified sources are stars, our stellar contamination rises to 14%. We test XDQSO by taking the same target density as identified by $giW1W2$ and find contamination rates of 17 – 42%, again depending on the nature of the non-ids.

Within our target redshift range we expect to find ≈ 75 quasars per 2dF pointing at this ($g < 20.5$) magnitude limit. In Table 1 we show the number of quasars identified by both algorithms as well as showing (in brackets) the number of quasars common to both. In the brighter regime ($g < 20.5$), we find that both algorithms identify at least 74 quasars within our target redshift interval and so both are consistent with being complete. However, we also note a further 9 quasars from the $giW1W2$ selection which corresponds to a 12% increase against the performance of XDQSO.

The single quasar ($g \leq 20.5$ & $0.8 < z < 2.5$) “missed” by $giW1W2$ is not detected in the All-Sky release and so was not missed due to incompleteness introduced as a result of our chosen colour selection. However, subsequent to our observations, an improved analysis of the WISE data (the ALLWISE data release) results in a detection for this target ($W1 = 17.07, S/N = 8.5$ and would be selected by our algorithm). This missing target suggests that our WISE photometry has an incompleteness for quasars within our target redshift range of $\sim 1\%$.

Some quasars are only identified by $giW1W2$ but not by XDQSO. Many of these would be found by our ugr colour selection, or a simpler colour-magnitude cut. The mean “probability” of these targets is $PQSO = 0.3$ and so would not be observable without a much higher fibre density. The XDQSO algorithm provides a “PQSO_ALLZ” parameter, that gives the “likelihood” of a target be-

Selection	Spectroscopic I.D.			
	QSO ($0.8 < z < 2.5$)	QSO ($0.3 < z < 3.5$)	Stars	Non-id
$giW1W2^\dagger$	84 (74)	106 (85)	3	12
XDQSO †	75	86	15	21
$giW1W2^\ddagger$	78 (39)	84 (40)	4	86
XDQSO ‡	74	77	4	93

Table 1. Here we show the relative performance of the XDQSO against a $giW1W2$ colour cut in a single 2dF with our highest completeness. We divide our comparison of the two algorithms into brighter objects $16 < g < 20.5$ (denoted by †) and fainter objects $20.5 < g < 22.5$ (denoted by ‡). Numbers are deg^{-2} and bracketed numbers show the number of quasars common to both selections.

ing a quasar at any redshift. For these “missed” quasars the mean “likelihood” is $\text{PQSO_ALLZ} = 0.8$. The low PQSO of these quasars is apparently caused by XDQSO attempting to estimate the redshift of the quasar candidates. The two red ($u-g > 0.7$) quasars detected by WISE are given low ratings by XDQSO ($\text{PQSO_ALLZ} = 0.81, 0.01$ and $\text{PQSO} = 0.26, 0.01$) and are therefore too lowly ranked by XDQSO to be observed.

In the fainter regime, XDQSO identifies a single quasar redder than $u-g=0.7$ of the 74 quasars within this redshift range. The $giW1W2$ selection recovers 9 (out of 78) with red optical colours. Combining the two selections we find that 9% of our sample in the fainter regime is “reddened” beyond the approximate limits of our $ugri$ colour selection.

We widen the redshift interval from $0.8 < z < 2.5$ to $0.3 < z < 3.5$, in the expectation that errors in redshift estimation performed by XDQSO will result in a high number of quasars outside the $0.8 < z < 2.5$ interval. We find that both algorithms select a significant number of quasars outside our targeted redshift range. For astrophysical studies of the quasar population this may not be an issue. However, to make the highest precision measurements of clustering, surveys require the highest density of quasars within as narrow a redshift interval as possible. Targeting quasars outside our preferred redshift interval lowers the efficiency of the survey.

We now examine spectroscopically confirmed quasars that are ranked as likely stars by the XDQSO algorithm. Given the continuous nature of the likelihood we make a cut in the output likelihood. We cut at $\text{PQSO} < 0.4$ as the target density above this value is $\approx 250 \text{ deg}^{-2}$, well above what is observable in a single epoch of spectroscopy with 2dF. After the $giW1W2$ selection, we find ≈ 10 quasars deg^{-2} (across all magnitudes), within our targeted redshift range that lie within this low PQSO region.

The mid-IR excess demonstrated by quasars places them in a region of colour space with a lower contamination rate than we see from XDQSO. If this contamination rate were to continue to fainter limits, then a mid-IR selection alone may be sufficient to achieve the target quasar density. With the current limits from the mid-IR photometry, which introduce photometric incompleteness, we must supplement the mid-IR selection with XDQSO to achieve higher quasar densities. In our sample field XDQSO recovers a quasar density of 54 quasars deg^{-2} ($0.8 < z < 2.5$, $g < 22.5$) compared to 74 quasars deg^{-2} from combining WISE, VSTATLAS and XDQSO.

5.4 The nature of mid-IR non-ids

Here we examine the contaminants within the $giW1W2$ colour space and attempt to discern the nature of the unidentified targets. We look both at the confirmed contaminants from a highly complete field and at the contaminants from the whole survey. Within the highly complete region (from Section 5.3) we have three spectroscopically confirmed stars with $g < 20.5$. These stars are identified as A and K-type stars from their spectroscopy and have been scattered up from the stellar locus. They are anomalously red in the $i-W1$ colour and hence included within our colour selection. Over the course of the survey we identified a number of white dwarfs (WDs) and M-type stars within our $giW1$ colour space. However, neither of these type of stars have broadband colours consistent with being identified by our $giW1$ selection. WDs have colour $i-W1 \lesssim 1$ and M stars have $g-i > 1.5$ so neither of these should contaminate the $giW1$ colour space.

The WIRED survey, Debes et al. (2011), categorised the infrared emission from UKIDSS Z-band to WISE W4 band of SDSS DR7 WDs. WDs with an infrared excess (mostly due to a contaminating M star) were identified as a potential source of the observed WD contamination of our colour space (see Debes et al. 2011). In Figure 3 we show that the WD+M star locus overlaps with the quasar locus in the $giW1$ colour space.

Debes et al. (2011) suggested that this may be due to the M-star contributing flux at longer wavelengths than the WD and thereby giving the system quasar colours. These authors found that $28 \pm 3\%$ WDs have M dwarf companions and approximately a further $\approx 2-10\%$ have either associated dust or a brown dwarf that would give them excess emission in the W1 band. Given the similar depths between SDSS and ATLAS we expect a similar rate of contamination as found by Debes et al. (2011).

To better examine the overlap between the quasar locus and the WD+M-star locus, we take our entire quasar sample and map its distribution in $giW1$ colour space in Figure 3. We show that the WD+M binaries directly overlap with the quasar locus in this colour space. Figure 3 explains the appearance of WDs and M stars in the $giW1$ colour cut. Whilst these systems will account for the occasional appearance of the spectroscopically confirmed contaminants, however, they do not have a sufficiently high sky density to account for the majority of the unidentified sources. We attempt to find a colour space that separates the stars and quasars that appear in the $giW1W2$ colour selection. If we are able to separate the stars and quasars by colour selection we may be able to infer the nature of the unidentified targets. We use all our observed targets to better characterise the contamination. In the right panel of Figure 4 we show the $gW1W2$ plane. We show as reference the position of the stellar locus, the locations of spectral type A and M stars, as well as the WDs with excess IR emission. We also show the quasar locus (derived from our whole sample). Spectroscopic stars and non-ids with $g < 20.5$ that obey our $giW1W2$ colour selection are also plotted. We see from the right panel of Figure 4 that the majority of stars may be removed by a cut in the $W1-W2$ colour. Due to the close proximity of the stellar locus, a cut in this colour may improve our efficiency but will affect our completeness as well. Where we have J-band coverage from the VHS survey (McMahon et al. 2013), we see from the left panel of Figure 4 that the $J-W1$ colour increases the separation between the stellar locus and the quasar locus. The majority of the non-ids lie within the quasar locus, although some do lie closer to the stellar locus. Table 2 quantifies that their mean $J-W1$ colours are consistent with quasar colours. Given that the number counts for non-ids peak a magnitude fainter than the peak

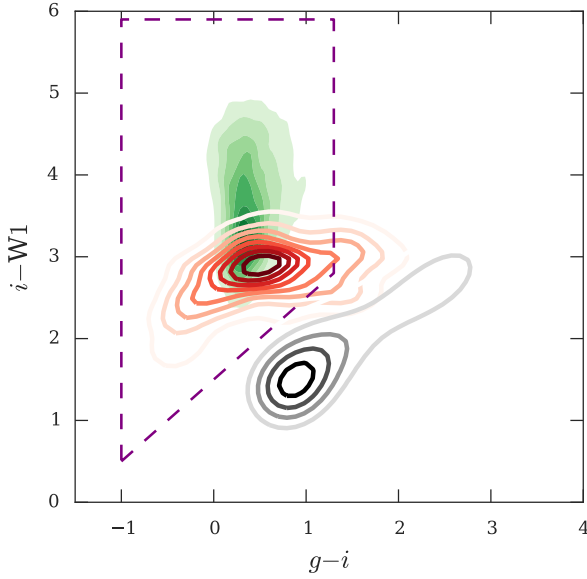


Figure 3. We show the distribution of our spectroscopic quasar sample, from the entire survey, in the $giW1$ colour space (green contour). We include morphological point-sources (identified by the g -band with $16 < g < 20.5$; shown as grey contour) and our $giW1$ colour cuts (dashed purple lines) from Section 4.0.5 for reference. We show that the WD+M binaries from Debes et al. (2011) (red contour) directly overlap with the quasar locus in this colour space acting to reduce the efficiency of this colour selection.

	QSO ($0.8 < z < 2.5$)	Stars	Non-id
$J - W1 > 1.5$	98% (3583)	22% (126)	92% (1311)
$J - W1 < 1.5$	2% (2)	78% (460)	8% (111)
$J - W1 > 2$	83%	13%	80%
$J - W1 < 2$	17%	87%	20%

Table 2. We show that the distribution in the $J - W1$ colour for spectroscopic quasars, stars and non-ids. At two different cuts, the distribution of the non-ids more closely follows that for quasars. As such, we infer that the greater part of the non-identified sources are quasars that are not positively identified by our spectroscopic observations.

of the identified targets, this suggests that many of these non-ids are quasars where positive identification has failed due to spectroscopic incompleteness.

5.5 Background stellar density

We find that the measured spectroscopic quasar density varies across the sky, independently of the selection algorithm (see Table A). Spectroscopic incompleteness will contribute to this variation. We minimise this by considering only sources with $g < 20.5$, where we are approximately complete. In Figure 5 we show the variation of confirmed quasars with $g < 20.5$ as a function of the number of point sources with $g < 21.5$ per square degree.

Figure 5 shows that the inverse correlation between stellar density and spectroscopic quasar density is the dominant cause of varying quasar density across the sky. This affect results in as much

as a factor of two between confirmed quasars in fields with different background stellar densities. This relation indicates that the efficiency of a wide area quasar survey depends on the background stellar counts in the observed fields.

However, we also note that the *ugriXDQSOW1W2* algorithm fields consistently identify a higher number density of quasars than the *ugriXDQSO* algorithm.

5.6 Conclusions

We combined mid-IR photometry from WISE with the *ugriz* photometry from the VST-ATLAS survey to improve the efficiency of our quasar selection. We found that the $giW1$ colour space (see Figure 1) is approximately complete to $g < 20.5$. Fainter than this the colour space becomes photometrically incomplete as quasars become too faint to be detected in the W1 band of WISE. We next attempted to use broadband colours to identify fainter (in the g -band) candidates from the $g-i : i-W1$ colour space that we were unable to identify from spectroscopy. Further analysis with the J-band failed to prove conclusively that the unidentified targets in this colour space were stars. These targets exhibit broad band colours consistent with quasars. This could mean that the colour space is complete to fainter limits in g than found in this work. We found that the combination of optical and mid-IR photometry improved the efficiency of our quasar selection. In Figure 5 we see that fields where WISE photometry was included in the quasar selection saw an increased yield of ≈ 10 quasars deg^{-2} . The improvement in quasar selection that we found in this survey may readily be extended to other quasar surveys in a similar redshift range such as eBOSS. Furthermore, we note that WISE photometry has proven to be a boon for quasar selection at higher redshifts (Carnall et al. 2015).

6 CLUSTERING ANALYSIS

6.1 Correlation function estimators

6.1.1 Redshift space correlation function

The two-point correlation function, $\xi(r)$, is commonly used to measure the excess probability of finding a pair of objects separated by distance r over a pair of randomly distributed objects. This probability is given by Peebles (1980) as;

$$dP = n^2 [1 + \xi(r)] dV_1 dV_2 \quad (1)$$

where n is the mean space density of objects and dV are volume elements around object 1 and 2. When measuring quasar positions we measure their distribution in redshift space and so we recover $\xi(s)$ instead of $\xi(r)$. To recover an estimate for $\xi(s)$ we use the estimator of Landy & Szalay (1993);

$$\xi_{LS}(s) = \frac{\langle DD \rangle - 2\langle DR \rangle + \langle RR \rangle}{\langle RR \rangle} \quad (2)$$

Here $\langle DD \rangle$ is the number of quasar-quasar pairs at a given separation, denoted by s . The $\langle DR \rangle$ and $\langle RR \rangle$ terms correspond to the number of quasar-random and random-random pairs respectively. To reduce the Poisson noise, we calculate the DR and RR terms from a much larger (twenty times larger) sample of randoms than we have quasars. It is necessary to normalise these terms by the measured quasar density. As discussed in Section 5.5 our measured quasar density varies by as much as a factor of two over the

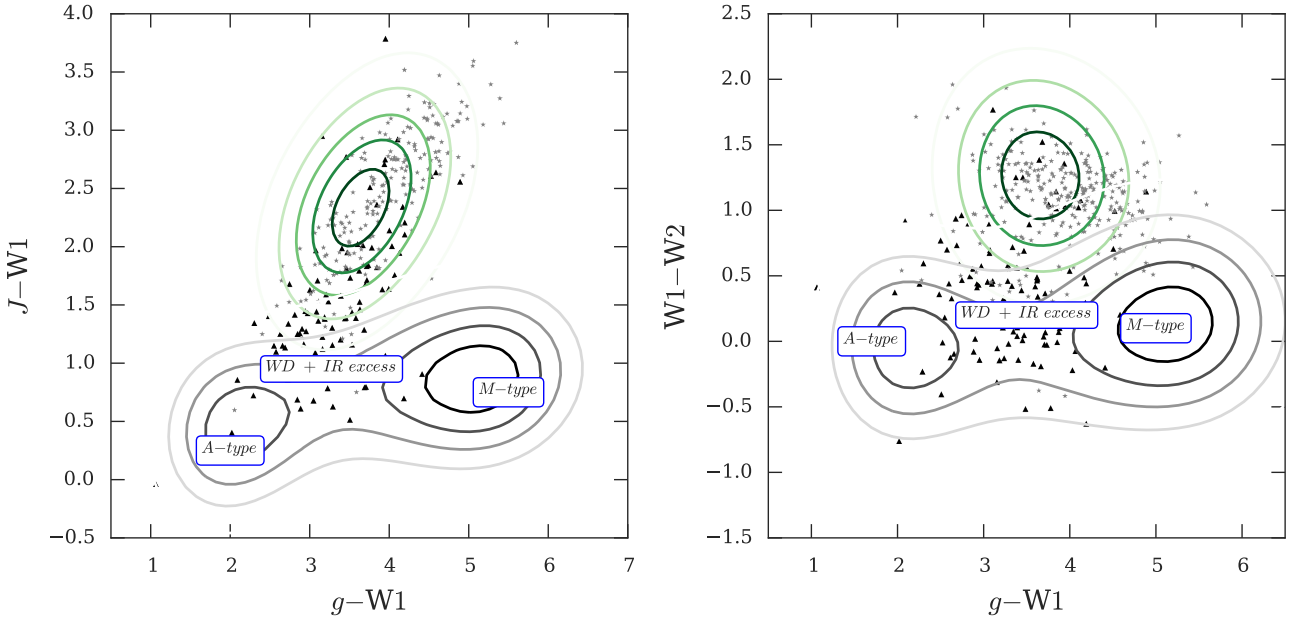


Figure 4. In the left panel we show the stellar locus in $gJW1$ colour space (grey contours). We also plot the locus of our quasar sample (green contours). Targets without a spectroscopic id that fulfil the $giW1W2$ colour cuts are shown as grey five point stars and spectroscopically confirmed stars are shown as black triangles. We also mark the location of spectral type A and M stars as well as the location of WD+IR excess stars from [Debes et al. \(2011\)](#). In the right panel we follow the same convention for marking the quasar and stellar locus, but instead show these in the $g-W1$ vs. $W1-W2$ colour space. The majority of non-ids have colours consistent with quasars in $giJW1W2$ photometric bands and suggest that the failure to positively identify these targets is due to spectroscopic incompleteness.

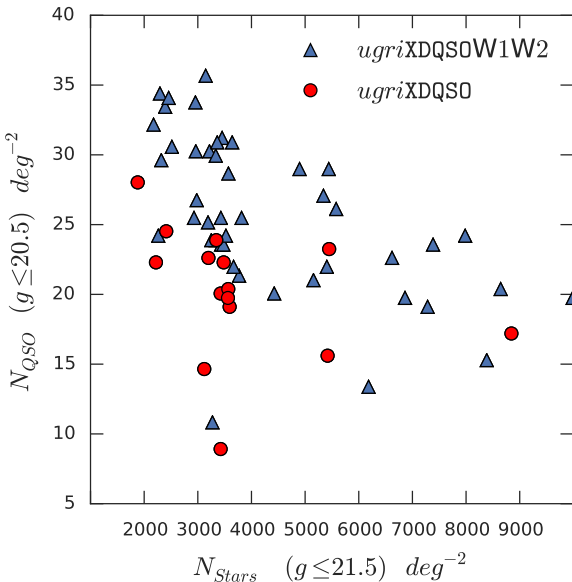


Figure 5. We show the number of confirmed quasars deg^{-2} ($g < 20.5$) against the number of stellar sources deg^{-2} (with $g < 21.5$). We compare the two algorithms; *ugriXDQSO* (red circles) and *ugriXDQSO W1W2* (blue triangles). By limiting the comparison to brighter quasars we assume the contribution of observational effects is negligible.

sky as a result of variation in our selection function and observing conditions. We therefore normalise our random sample on a field by field basis dependent on the total number of quasars in a given field. This normalisation should help counter effects of photometric and spectroscopic incompleteness. Assuming quasar clustering to be described by a power-law with a correlation scale of $r_0 = 6.1 h^{-1} \text{Mpc}$ and slope $\gamma = 1.8$ the affect of the integral constraint from a single 2dF field is sufficiently small to have little effect on our measurements and only affects clustering measurements on the largest ($\approx 100 h^{-1} \text{Mpc}$) physical scales.

6.1.2 Modelling quasar clustering in redshift space

Following the methodology of other quasar surveys ([da Ângela et al. \(2005\)](#), [dA08](#)) we define $\xi(s) = \xi(\sigma^2 + \pi^2)$ where σ is the pairwise separation perpendicular to the line of sight and π is parallel to the line of sight and

$$1 + \xi(\sigma, \pi) = \int_{-\infty}^{\infty} [1 + \xi'(\sigma, \pi - w_z(1+z)/H(z))] f(w_z) dw_z \quad (3)$$

and $\xi'(\sigma, \pi - w_z(1+z)/H(z))$ is given by equations 12-14 of [da Ângela et al. \(2005\)](#). These equations are completely equivalent to modelling the linear z-space distortions via the ‘Kaiser boost’ of $\xi(s) = \xi(r(1 + 2/3\beta + 1/5\beta^2))$ where $\beta(z) = \Omega_m(z)^{0.6}/b(z)$ is the infall parameter and $b(z)$ is the bias. $f(w_z)$ is the distribution of pairwise peculiar velocities, w_z , that includes the small-scale clustering motions of the quasars. From the above we can then derive $\xi(s)$ where $s = \sqrt{\sigma^2 + \pi^2}$. Fitting $\xi(s)$ will form our main route to measuring quasar clustering amplitudes. We fit the correlation function

between $5 < s (h^{-1} \text{Mpc}) < 55$ and assume a power-law model for $\xi(r)$ with $\xi(r) = (r/r_0)^{-\gamma}$ and with a fixed $\gamma = 1.8$.

At small scales ($s \lesssim 5 h^{-1} \text{Mpc}$) redshift space distortions dominate the clustering signal in $\xi(s)$. Non-linear, ‘finger-of-God’ peculiar velocities of the quasars and redshift measurement errors both act to reduce $\xi(s)$ at these scales. Justified mainly by the good fit it provides, we shall assume a Gaussian for $f(w_z)$ (see Ratcliffe 1996) with a fixed velocity dispersion of $\langle w_z^2 \rangle^{\frac{1}{2}} = 750 \text{ km s}^{-1}$.

To fit $\xi(s)$ we need an initial model for quasar bias and its dependence on redshift. We shall assume the previous 2QZ fit of C05;

$$b = 0.53 + 0.289(1+z)^2. \quad (4)$$

This implies a $\pm 10\%$ difference to $1 + 2/3\beta(z)$ in the $0.5 < z < 2.5$ range wrt. the median redshift $z=1.4$. This corresponds to a $\pm 5\%$ effect in r_0 . Therefore, we cannot assume that β is independent of redshift in fitting $\xi(s)$ for r_0 . We fit $\xi(s)$ using the above model for bias and we shall check for consistency with our new results for the z dependence of bias at the end of our analysis.

6.2 2QDESp Quasar correlation function

We present the z -space two point correlation function, $\xi(s)$, measured from the 2QDESp sample for $0.3 \leq z \leq 3.5$ in Figure 6. Widening the redshift interval from our targeted redshift range ($0.8 < z < 2.5$) maximises the signal of the correlation function. We have considered two estimates of the errors, Poisson and jackknife. At small enough scales and sparse enough space densities, it is well known that the errors in ξ can be approximated by Poisson errors. Usually measured as $\Delta\xi(s) = 1 + \xi(s) / \sqrt{\langle DD \rangle}$, which is the error assuming that the clustering signal is zero. However, in cases where value of $\xi(s)$ is negative, this estimate under predicts the error. In these cases we model the Poisson error to be;

$$\Delta\xi(s) = \sqrt{\frac{1 + \xi(s)_{\text{MODEL}}}{\langle DR \rangle_{\text{observed}}}} \quad (5)$$

When a bin in s is well populated with quasar-quasar pairs this error estimate and the Poisson error approximately converge. The error estimate of equation 5 is used only within Section 6.3.2 due to the s bins being more sparsely sampled. We note that this error appears insensitive to a range of model r_0 values and is instead sensitive to the $\langle DR \rangle_{\text{observed}}$ value.

At these smaller scales, the covariance between ξ estimates may be ignored in fits on the basis that the pair counts are close to being independent. We demonstrate this by comparing jackknife and Poisson errors for 2QDESp. To calculate the jackknife errors, we split the data into ≈ 60 subsamples (each separate 2dF pointing) and calculate the error using a jackknife approach described by:

$$\sigma_{\text{jackknife}} = \sqrt{\sum_{i=1}^N \frac{DR_i(s)}{DR_{\text{total}}(s)} (\xi_i(s) - \xi_{\text{total}}(s))^2}, \quad (6)$$

where N is the total number of subsamples, the i subscript denotes which 2dF field has been removed from the whole sample and the total subscript denotes use of the full sample. Here we weight each term within the sum by the number of data-random pairs excluded from the calculation and so weight more densely sampled fields more highly than those with fewer data random pairs.

For comparison, we show the ratio of the jackknife error estimation to Poisson errors in the top panel of Figure 6. We see that the Poisson error is a reasonable representation of the jackknife error out to $s < 30 h^{-1} \text{Mpc}$ and is still within a factor of ≈ 1.4 at

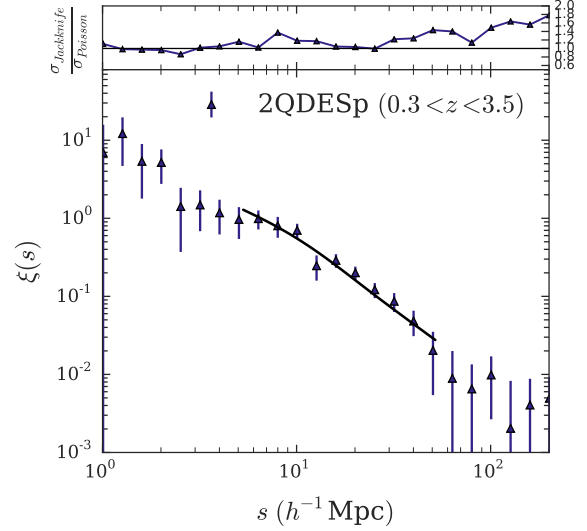


Figure 6. We show the measured $\xi(s)$ for the 2QDESp quasar sample between $0.3 < z < 3.5$. We include our model with best-fitting correlation length (using Jackknife errors) of $r_0 = 6.25 \pm 0.30 h^{-1} \text{Mpc}$. In the top panel, we show the ratio between the Jackknife and Poisson errors.

$s < 55 h^{-1} \text{Mpc}$, only reaching a factor of ≈ 1.8 at $s \approx 100\text{--}200 h^{-1} \text{Mpc}$. This suggests that, at least out to $s < 55 h^{-1} \text{Mpc}$, pair counts are reasonably independent and this is supported by the small size of off-diagonal terms in the covariance matrix at these scales. We shall fit models in the range $5 < s < 55 h^{-1} \text{Mpc}$ using both jackknife and Poisson errors.

We now fit the model from Section 6.1.2 to the 2QDESp $\xi(s)$ data. We show our best-fitting model assuming Poisson errors in the lower panel of Figure 6. This has $r_0 = 6.25 \pm 0.25 h^{-1} \text{Mpc}$ which fits well with $\chi^2 = 9.4$ with 10 degrees-of-freedom, (df.). Assuming jackknife errors for the fit gives a similar result, $r_0 = 6.25 \pm 0.30 h^{-1} \text{Mpc}$ ($\chi^2, \text{df.} = 7.0, 10$).

To further test the quality of our data, we divide the quasar sample into three subsets, based on the quality of their optical spectra. The three subsets consist of 1675, 4585 and 3541 quasars for the highest, intermediate and lowest quality spectra respectively. We compare the different quality spectra in Figure 7, where we plot the correlation function for the three quasar subsamples. We fit the model from Section 6.1.2 to each and find that the three subsamples agree at the $\sim 1\sigma$ level. Using this procedure we verify that our lowest quality optical spectra are suitable to use in our science measurements as the contamination by other sources is low enough not to cause significant differences in the measured clustering signal.

6.3 Luminosity dependence of clustering

In this section we search for evidence of luminosity dependent quasar clustering. We start with the approach of S11 and compare measured r_0 values between different surveys at approximately fixed redshift. We follow this with the more precise methodology of dA08 which divides the samples by absolute magnitude and redshift. We defer measurement of redshift dependence to Section 6.4.

Survey	$r_0(h^{-1}\text{Mpc})$ ($\gamma = 1.8$)	Faint limit	Median mag. (g)	Median z	N_{QSO}	$\chi^2(10df.)$ ($r_0 = 6.1h^{-1}\text{Mpc}$)
SDSS	$6.55^{+0.30}_{-0.30}$	$g < 19.4$	18.8	1.37	32650	4.7
2QZ	$5.85^{+0.20}_{-0.20}$	$g < 20.8$	20.1	1.48	22211	14.9
2QDESp	$6.10^{+0.25}_{-0.25}$	$g < 22.5$	20.6	1.54	9705	12.1
2SLAQ	$6.15^{+0.35}_{-0.35}$	$g < 21.9$	21.3	1.58	6374	15.6

Table 3. We present model fits for the re-analysed data sets, 2QZ, 2SLAQ and SDSS DR5 as well as for the 2QDESp sample. We restrict our analysis to quasars between $0.3 < z < 2.9$ to ensure good agreement between the redshift distributions. We include the best-fitting r_0 , the faint limits of the quasar samples as well as their median magnitudes, redshifts and number of quasars. We note that limiting our analysis (in the case of 2QDESp) to this redshift interval changes the best fitting value compared to Section 6.2. However, this change is $< 1\sigma$ and is discussed in Section 6.4.

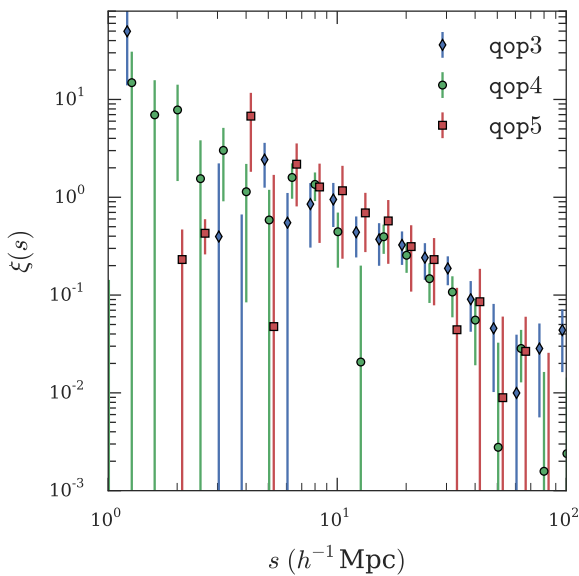


Figure 7. Here we show the correlation function for 2QDESp quasars with the highest, intermediate and lowest quality spectra, qop = 5, 4 and 3 respectively. We offset the high and low spectral quality correlation functions along the x-axis by $10^{s \pm 0.02}$ for clarity. The three correlation functions for each quality level agree. Hence we argue that the lowest quality sample is suitable for use in our analysis.

6.3.1 Apparent magnitude

Comparison between the 2QZ, SDSS, 2SLAQ and 2QDESp quasar surveys provides an opportunity to measure the dependence of clustering on luminosity. Whilst each survey has different selection methods and flux limits we see in Figure 2 that the resulting redshift distributions are similar (see also Table 3). Given that each survey is flux limited, we account for photometric and spectroscopic incompleteness by characterising each survey by its median magnitude. For the four surveys this corresponds to; $g=18.8$ (SDSS), $g=20.1$ (2QZ, see Richards et al. (2005) for $b_J - g$ conversion), $g=21.3$ (2SLAQ) and $g=20.6$ for the 2QDESp sample.

In Figure 8 we show our re-analysis of the SDSS, 2QZ, 2SLAQ and 2QDESp clustering results, restricting our analysis to quasars between $0.3 < z < 2.9$. We have rebinned the s -axis to a common binning across the four surveys. In each panel we show the

best-fit r_0 for each survey, assuming a fixed β . We permit use of constant β here because with the small difference in median redshifts the effect of different $\beta(z)$ values will have $< 1\%$ effect on r_0 . Our best-fitting values are shown in Table 3 and these measurements agree with the analysis of S11 with any differences in the best-fit values due to slight difference in redshift range and fitting interval.

We make a comparison between the median magnitude and best-fit values of r_0 across the four surveys in Figure 9. We note that Shen et al. (2009) found that the brightest SDSS DR5 quasars clustered more strongly than the rest of their quasar sample. We find here that r_0 for the SDSS quasars is larger than the r_0 values from the other surveys but only at $\approx 1\sigma$ level. As this effect corresponds to the result reported by Shen et al. (2009) we must be cautious not to immediately dismiss the difference as purely statistical. However, we further test for the dependence on r_0 with magnitude using the Spearman rank correlation test. We find a Spearman rank order correlation of $\rho = -0.19 \pm 0.37$ which is consistent with no correlation between apparent magnitude and clustering scale. We also find that the points in Figure 9 are consistent with a constant $r_0 = 6.10^{+0.10}_{-0.10} h^{-1}\text{Mpc}$ with $\chi^2, df. = 3.9, 3$ and p-value = 0.28.

In Table 3 we calculate the corresponding χ^2 when we compare each survey individually to a fixed $r_0 = 6.1 h^{-1}\text{Mpc}$ and we find that the total $\chi^2, df. = 46.8, 40$ (we include the individual survey χ^2 values in Table 3). So from this analysis we are unable to reject the hypothesis that quasar clustering is independent of luminosity from a comparison between the individual surveys.

6.3.2 Absolute magnitude

In Section 6.3.1 we compared quasar clustering over a range of ~ 3.5 magnitudes at fixed redshift. Although further subdivision of the quasar samples will yield weaker statistical constraints, we are, however, able to probe a much larger dynamic range ($-22.3 < M_i(z=2) < -28.5$) at fixed redshift by combining all four surveys. We do this by taking the error weighted mean of the four correlation functions for each subsample. Following the approach of dA08, we divide the M - z plane into non-overlapping bins. We use the sample binning of dA08 which was designed to maximise the clustering signal from the 2QZ+2SLAQ combined sample. The inclusion of the SDSS and 2QDESp data reduces the statistical errors; particularly in the highest and lowest luminosity bins. This may enable us to potentially uncover previously hidden dependencies.

We therefore subdivide the quasar samples into thirteen, non-overlapping subsets in luminosity and redshift. The absence of low-luminosity quasars at high redshift limits the dynamic range (in

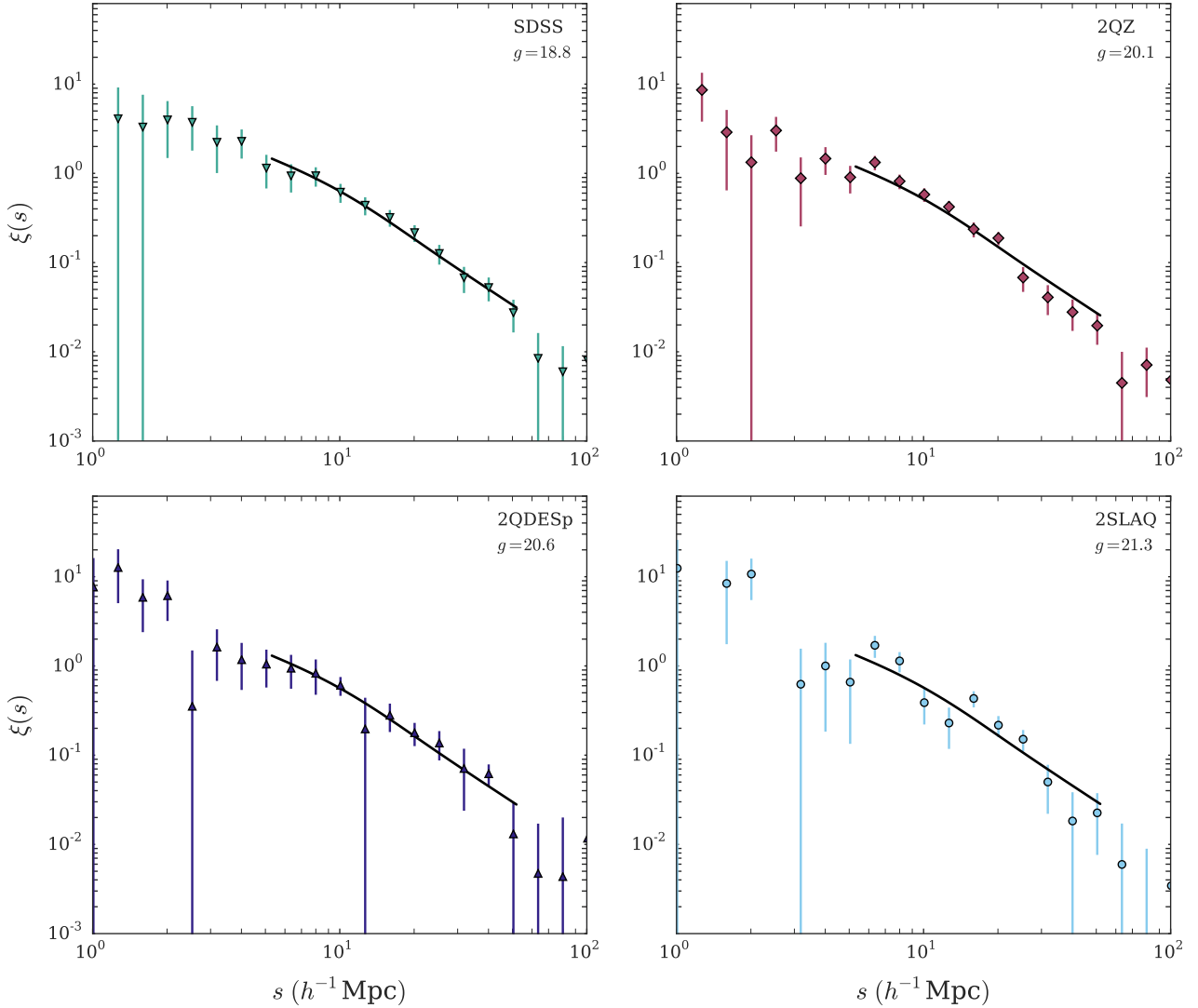


Figure 8. Each panel shows our estimate of $\xi(s)$ measured for a particular wide area survey as labelled. We annotate each panel with the median magnitude in g for comparison to our survey. Errors are Poisson. We fit the data using the model from section 6.1.2, where we assume Gaussian velocity dispersions in real space, $\gamma = 1.8$ with a velocity dispersion, $\langle \omega^2 \rangle^{\frac{1}{2}} = 750 \text{ km s}^{-1}$. In each panel we show the model where $r_0 = 6.1 \text{ h}^{-1} \text{ Mpc}$ (solid line) (see section 6.1.2). For each survey we restrict the analysis to the redshift interval $0.3 < z < 2.9$ as this range is well sampled by all surveys. The best-fitting models for the individual surveys are shown in Table 3.

luminosity) at the higher redshifts. We calculate the absolute magnitudes M_i using

$$M_i = i - A_i - 25 - 5 \log(d) - K_i, \quad (7)$$

where i is the apparent magnitude, A_i is the dust extinction, d is the luminosity distance in Mpc and K_i is the k -correction in the i -band. The galactic dust correction, A_i is calculated by $A_i = 2.086 E(B - V)$ (Schlegel et al. 1998). The k -correction value was taken from Richards et al. (2006).

We show the distribution of the 2QDESp sample in the left hand panel of Figure 10. We overlay the Figure with the M - z divisions and include the occupancy of each division. In the right panel of Figure 10 we plot the M - z distribution for the combined (SDSS+2QZ+2SLAQ+2QDESp) sample. Again, we overlay the M - z divisions and show the total bin occupancy. In both panels of Figure 10 the flux limited nature of the surveys is evident by the ab-

sence of lower luminosity quasars at higher redshifts. As expected, we see that the 2QDESp survey makes its largest contribution at fainter absolute luminosities.

Our aim in subdividing the combined sample in both magnitude and in redshift is to isolate redshift and luminosity dependent effects on the clustering amplitude. In Figure 11 we show the signal for each of the absolute magnitude and redshift bins. To generate random samples we use R.A.-Dec. mixing (see C05), sampling from the all magnitudes and redshifts to generate the angular mask. The radial mask is generated by randomly sampling the redshift distribution of the magnitude-redshift subsample. We found that fitting the radial distribution with a polynomial provided similar results to those included here.

Previously we fit for r_0 at approximately fixed redshift. However, here we are fitting over $\Delta z \sim 1.7$ and so an assumption of constant β is no longer valid. We therefore measure the correlation

Redshift range	z (median)	Absolute magnitude range $M_i(z=2)$	$M_i(z=2)$ (median)	Best r_0	χ^2	p-value	ξ_{20}	b	$M_{DM} \times 10^{12} h^{-1} M_\odot$
$0.3 < z < 0.8$	0.53	$-23.5 < M_i < -22.3$	-23.06	$4.2^{+0.65}_{-0.8}$	11.96	0.29	0.18 ± 0.06	–	–
$0.8 < z < 1.4$	0.99	$-23.5 < M_i < -22.3$	-23.18	$5.65^{+1.2}_{-1.0}$	5.95	0.82	0.39 ± 0.11	1.79 ± 0.29	$3.60^{+3.54}_{-2.19}$
$0.3 < z < 0.8$	0.63	$-24.5 < M_i < -23.5$	-23.93	$4.05^{+0.8}_{-1.05}$	8.7	0.56	0.25 ± 0.08	1.13 ± 0.21	$0.71^{+1.60}_{-0.62}$
$0.8 < z < 1.4$	1.10	$-24.5 < M_i < -23.5$	-24.04	$5.65^{+0.7}_{-0.9}$	8.91	0.54	0.29 ± 0.08	1.58 ± 0.24	$1.40^{+1.55}_{-0.90}$
$1.4 < z < 1.9$	1.61	$-24.5 < M_i < -23.5$	-24.15	$7.1^{+0.8}_{-0.9}$	10.77	0.38	0.40 ± 0.10	2.39 ± 0.33	$2.87^{+2.08}_{-1.43}$
$1.9 < z < 2.9$	2.02	$-24.5 < M_i < -23.5$	-24.31	$9.1^{+2.7}_{-3.65}$	9.26	0.51	1.08 ± 0.43	4.79 ± 0.96	$17.17^{+13.55}_{-9.23}$
$0.3 < z < 0.8$	0.69	$-25.5 < M_i < -24.5$	-24.84	$4.4^{+1.5}_{-2.1}$	13.0	0.22	0.37 ± 0.15	1.51 ± 0.34	$3.62^{+6.18}_{-2.92}$
$0.8 < z < 1.4$	1.07	$-25.5 < M_i < -24.5$	-25.09	$4.3^{+0.7}_{-0.75}$	13.98	0.17	0.21 ± 0.06	1.29 ± 0.21	$0.42^{+0.72}_{-0.33}$
$1.4 < z < 1.9$	1.65	$-25.5 < M_i < -24.5$	-24.99	$5.6^{+0.7}_{-0.85}$	8.84	0.55	0.36 ± 0.08	2.28 ± 0.27	$2.10^{+1.35}_{-0.96}$
$1.9 < z < 2.9$	2.11	$-25.5 < M_i < -24.5$	-25.07	$6.55^{+0.95}_{-1.1}$	5.52	0.85	0.33 ± 0.11	2.60 ± 0.44	$1.36^{+1.33}_{-0.81}$
$0.8 < z < 1.4$	1.21	$-28.5 < M_i < -25.5$	-25.94	$5.85^{+0.6}_{-0.6}$	9.08	0.52	0.34 ± 0.07	1.84 ± 0.21	$2.27^{+1.52}_{-1.06}$
$1.4 < z < 1.9$	1.67	$-28.5 < M_i < -25.5$	-26.27	$5.85^{+0.35}_{-0.4}$	16.98	0.07	0.37 ± 0.04	2.35 ± 0.15	$2.28^{+0.71}_{-0.59}$
$1.9 < z < 2.9$	2.19	$-28.5 < M_i < -25.5$	-26.58	$6.2^{+0.45}_{-0.5}$	7.63	0.67	0.39 ± 0.05	2.91 ± 0.20	$1.90^{+0.62}_{-0.51}$

Table 4. We show the best-fit value of r_0 for each $M - z$ bin with the corresponding error, χ^2 and p-value. We correct for varying $\beta(z)$ according to equation 4. We fit between $5 < s < 55$ (h^{-1} Mpc), each bin having 10 df.. We include measurements of ξ_{20} (section 6.4), bias and dark matter halo mass (section 6.4.1).

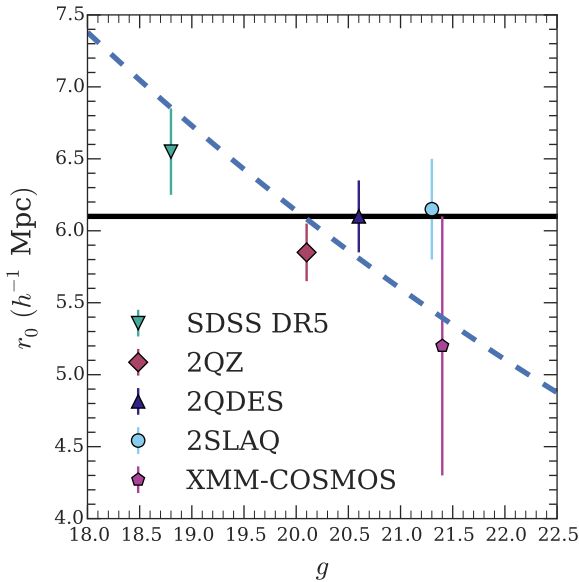


Figure 9. We show the median depth for 2QZ, 2SLAQ, SDSS and 2QDES surveys along with the best-fit r_0 with the associated errors. We also show a flat $r_0 = 6.1 h^{-1}$ Mpc model (solid line) and a $L^{0.1}$ model (dotted line).

function for each subsample in Figure 11 but determining $\beta(z)$ from an assumed $b(z)$ relationship (see equation 4). Whilst there is uncertainty in the precise form of the $b(z)$, a 50% increase in bias at $z = 1.5$ only results in a 4% change in r_0 .

Allowing the value of r_0 to vary between each bin we find a total $\chi^2, \text{df.} = 130.6, 130$ and p-value = 0.47. We plot the best-fit values (see Table 4) in Figure 12. We also include in this Figure our determination of r_0 from the measured $\xi(s)$ of Eftekharzadeh et al. (2015); using our model we find their correlation function corresponds to $r_0 = 7.25 \pm 0.1 h^{-1}$ Mpc.

In Figure 12 we compare across the luminosity bins at approximately fixed redshift. The fainter two magnitude bins (spanning $-24.5 < M_i < -22.3$) show, on average, stronger clustering at all redshifts than the brighter bins. If this trend is physical it would suggest that fainter quasars are more strongly clustered than brighter quasars, suggesting an inverse relationship between quasar lumi-

nosity and halo mass. However, we note that these magnitude-redshift bins correspond to the faintest apparent magnitudes in the 2QDES and 2SLAQ samples and suffer from large incompleteness. So although there may be a weak underlying dependence on luminosity we are unable to claim a significant detection analysing the data in this fashion. It is possible, of course, that some effect of luminosity dependence is being masked by the redshift dependence of quasar clustering.

6.4 Redshift dependence

In Figure 12 we see evidence for redshift dependence of quasar clustering and find that the increase in r_0 with redshift is significantly detected using the Spearman rank order correlation test ($\rho = 0.82 \pm 0.18$). Here we attempt to measure the evolution of quasar clustering with redshift. Following the methodology of earlier authors (C05; dA08) we use the integrated correlation function. We measure the clustering excess up to some radius ($s < 20 h^{-1} \text{Mpc}$) and normalise the signal according to the average quasar numbers contained within a $20 h^{-1} \text{Mpc}$ radius sphere;

$$\xi_{20} = \frac{3}{20^3} \int_0^{20} \xi(s) s^2 ds \quad (8)$$

C05 in particular looked at the effect of both systematic and statistical uncertainties associated with integrating different radius spheres. We adopt the same radius as used by these authors (see C05, for a detailed analysis).

In Figure 13 we show the integrated correlation function for each absolute magnitude and redshift bin from Section 6.3.2. We show the redshifts and ξ_{20} values for these bins in Table 4. We see that the evolution of $\xi_{20}(z)$ is flatter than one might naively expect from either Table 4 or Figure 12. This is due to the effect of $\beta(z)$, accounted for in our model, that “boosts” $\xi_{20}(z)$ more at lower redshifts than at higher redshifts and thus flattens the evolution of ξ_{20} .

6.4.1 Bias & Halo Masses

2QZ measured the quasar correlation function as a function of redshift (see C05). They reported the relationship of quasar bias with redshift described by equation 4. In this section we use the same methodology as previous works (C05; dA08 and R09) with our larger dataset to more precisely determine the evolution of bias with redshift.

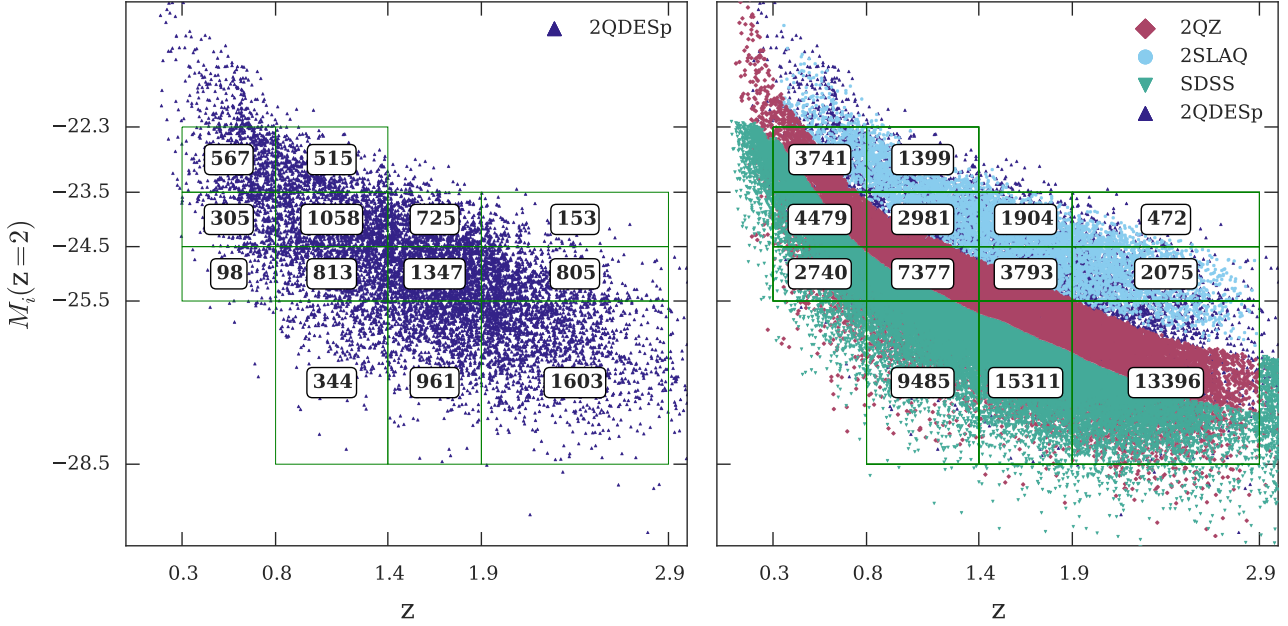


Figure 10. The distribution of our sample in redshift-luminosity (left) and the comparison to 2QZ, 2SLAQ, SDSS DR5 and 2QDESp surveys (right). The grids show the division in magnitude and redshift applied to the samples and the occupancy of each bin.

We assume a scale independent bias and thus obtain;

$$b = \sqrt{\frac{\xi^Q(r)}{\xi^P(r)}} \simeq \sqrt{\frac{\xi_{20}^Q}{\xi_{20}^P}}, \quad (9)$$

where $\xi^Q(r)$ and $\xi^P(r)$ are the quasar and matter real space correlation functions, with ξ_{20}^Q and ξ_{20}^P being the corresponding integrated correlation functions to $s < 20h^{-1}$ Mpc. Kaiser (1987) describes the relation between the real and z -space correlation functions on linear scales as

$$\xi_{20}^Q(s) = \left(1 + \frac{2}{3}\beta + \frac{1}{5}\beta^2\right)\xi_{20}^P(r). \quad (10)$$

This results in an expression for quasar bias as a function of redshift;

$$b(z) = \sqrt{\frac{\xi_{20}^Q(s)}{\xi_{20}^P(r)}} = \sqrt{\frac{4\Omega_m^{1.2}(z)}{45} - \frac{\Omega_m^{0.6}}{3}}. \quad (11)$$

In line with earlier work we use 0.6 as the exponent to Ω_m . To estimate $\xi_{20}^P(r)$ we use the matter power-spectrum at $z = 0$. This was calculated using CAMB (Lewis et al. 2000; Challinor & Lewis 2011), which is based on CMBFAST (Seljak & Zaldarriaga 1996; Zaldarriaga & Seljak 2000). Under our assumed cosmology we find $\xi_{20}^P(r) = 0.253$ at $z = 0$. We can then use linear theory to convert from a measured ξ_{20}^Q to bias (b) via equation 9. We correct for non-linear effects in the same manner as described by C05.

Figure 14 shows how the resulting bias varies with z . We fit an empirical relationship to the results in Figure 14;

$$b(z) = (0.59 \pm 0.19) + (0.23 \pm 0.02)(1 + z)^2. \quad (12)$$

We note that this z dependence has the same quadratic form than

that of equation 4 but with a weaker gradient. We refer back to Section 6.3.2 where we discussed the effect of different $b(z)$ models on the measurement of r_0 . We remeasure the r_0 fits from earlier sections and find changes in the best-fit values are of the order $\pm 0.05 h^{-1}$ Mpc, well below our statistical error.

Figure 13 shows the difference the change in the $b(z)$ relationship makes on ξ_{20} . The dashed line showing the prediction of ξ_{20} from $\xi_P(r, z = 0)$ and equation 4 and the solid line showing the prediction of equation 12. We also plot the independent BOSS data from Eftekharzadeh et al. (2015) which lies much closer to our $b(z)$ result than that of 2QZ.

Having derived bias values from our measured values of $\xi_{20}^Q(s)$ (see Table 4) we want to relate these values to the mean halo mass of the host halos. Sheth et al. (2001) extended the formalism of Mo & White (1996) to account for the ellipsoidal collapse of dark matter halos. This gives the relation between bias and halo mass,

$$b(M, z) = 1 + \frac{1}{\sqrt{a}\delta_c(z)} \left[av^2 \sqrt{a} + 0.5 \sqrt{a}(av^2)^{1-c} - \frac{(av^2)^c}{(av^2)^c + 0.5(1-c)(1-c/2)} \right], \quad (13)$$

where $v = \delta_c/\sigma(M, z)$, $a = 0.707$ and $c = 0.6$. δ_c is the critical overdensity for the collapse of a homogeneous spherical perturbation, given by $\delta_c = 0.15(12\pi)^{2/3}\Omega_m(z)^{0.0055}$, (Navarro et al. 1997). We describe the variance in the mass fluctuation of the density field for a mass scale M as $\sigma(M)$

$$\sigma^2(M) = \frac{1}{2\pi^2} \int_0^\infty k^2 P(k) w^2(kr) dk, \quad (14)$$

where $P(k)$ is the matter power spectrum and

$$w(kr) = \frac{3(kr \sin(kr) - \cos(kr))}{(kr)^3}, \quad (15)$$

is the Fourier transform of a spherical tophat (Peebles 1980). Ra-

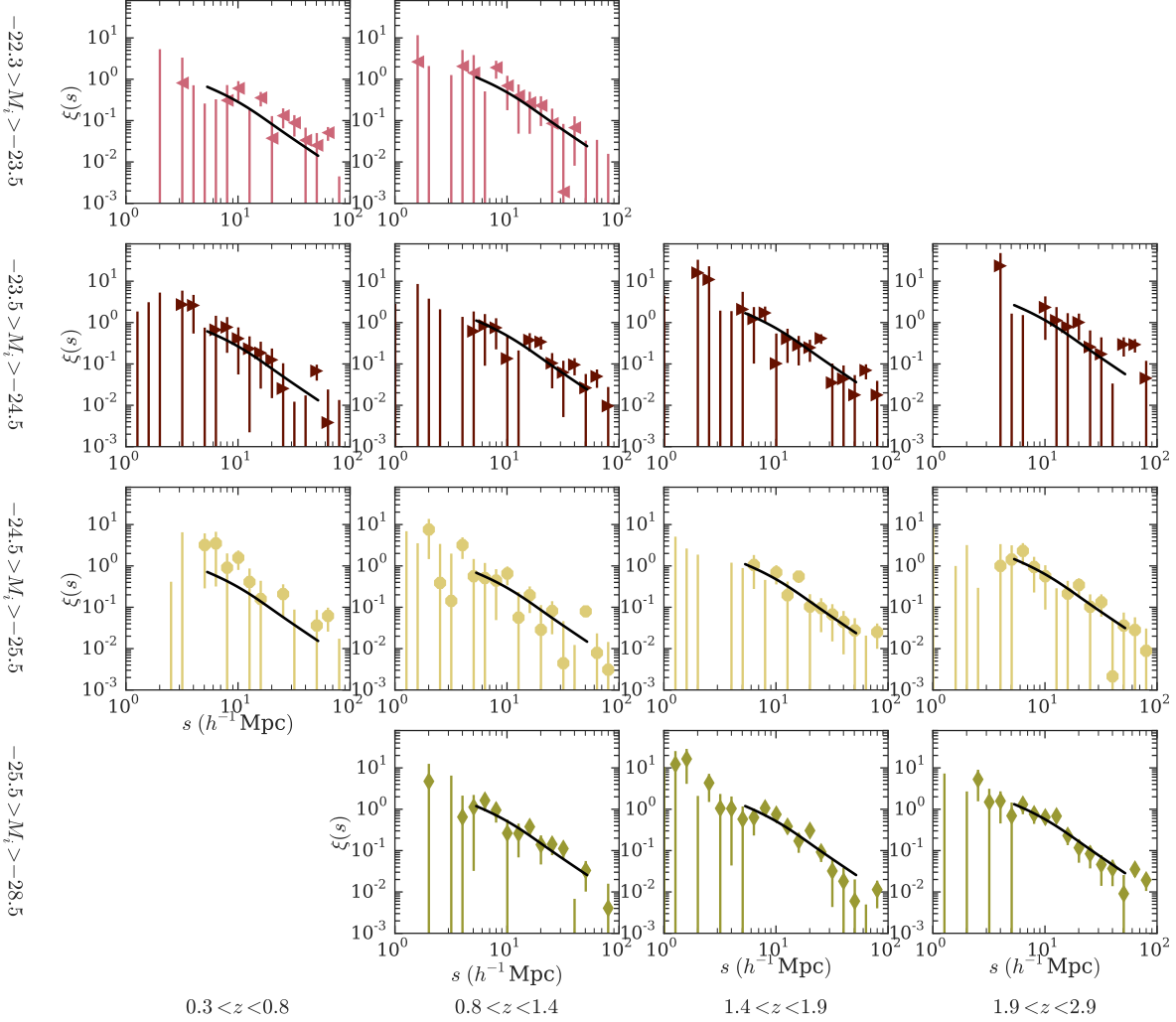


Figure 11. We measure the correlation function $\xi(s)$ for the combined sample (SDSS, 2QZ, 2SLAQ and 2QDES) in the same bins as Figure 10. We use the error weighted mean to combine the measurements from each individual survey, where errors are Poisson (see Section 6.2). These are compared to a $\xi(s)$ model where $r_0 = 6.1 h^{-1} \text{ Mpc}$ (solid line). We show the fit quality for this fixed r_0 value as well as for the best-fitting value in Table 4.

dus r is related to mass by

$$r = \left(\frac{3M}{4\pi\rho_0} \right)^{\frac{1}{3}}, \quad (16)$$

where ρ_0 is the mean density of the Universe at $z = 0$, $\rho_0 = 2.78 \times 10^{11} \Omega_m^0 h^2 \text{ M}_\odot \text{ Mpc}^{-3}$. We calculate the rms mass fluctuation at a given redshift using the linear growth factor $D(z)$

$$\sigma(M, z) = \sigma(M) D(z). \quad (17)$$

We show the bias values and associated halo masses in Table 4. In Section 6.3.2 we found little signal of a luminosity dependence of quasar clustering from our measurements of r_0 . We compare the halo masses for different magnitude bins to re-examine those results. It is at higher redshift that we are best able to distinguish between different mass halos from their bias values as such we ex-

clude the faintest luminosity bin as there was no data at higher redshifts.

The clustering of the remaining three magnitude bins is best described by halo masses of $6 \pm 8 \times 10^{12} h^{-1} \text{ M}_\odot$, $1.9 \pm 1.4 \times 10^{12} h^{-1} \text{ M}_\odot$ and $2.2 \pm 0.2 \times 10^{12} h^{-1} \text{ M}_\odot$ (rms error) for the $-24.5 < M_i < -23.5$, $-25.5 < M_i < -24.5$ and $-28.5 < M_i < -25.5$ bins respectively.

We find that (excluding the high- z , low- M bin) the evolution of bias with redshift is well described by a mean halo mass of $M = 2 \pm 1 \times 10^{12} h^{-1} \text{ M}_\odot$ (c.f. $M = 3 \pm 5 \times 10^{12} h^{-1} \text{ M}_\odot$ including this bin). We show the model prediction for this halo mass in Figure 14 as a solid line. Within the errors, our bias measurements are consistent with a single halo mass at all redshifts and luminosities.

Our measurement of the evolution of $b(z)$ is slightly different than that of C05, the determination of halo mass has large errors.

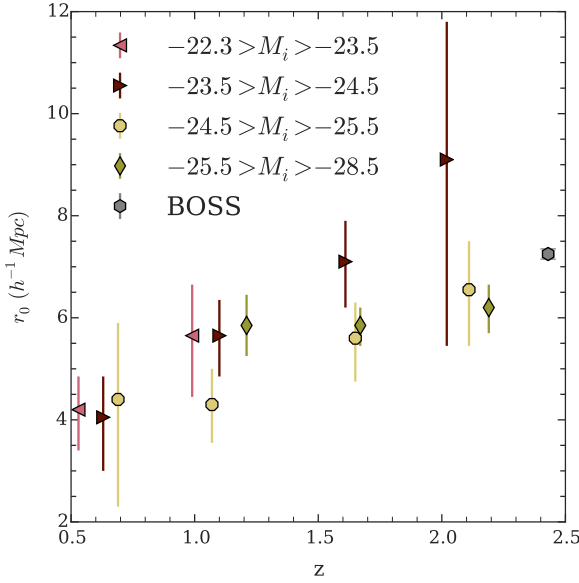


Figure 12. We show the measured correlation length (r_0) for the thirteen luminosity–redshift bins from Table 4. We include our measurement of r_0 from the correlation function of Eftekharzadeh et al. (2015) who measure the clustering scale of quasars from the BOSS sample as $r_0 = 7.25 \pm 0.10 h^{-1}$ Mpc.

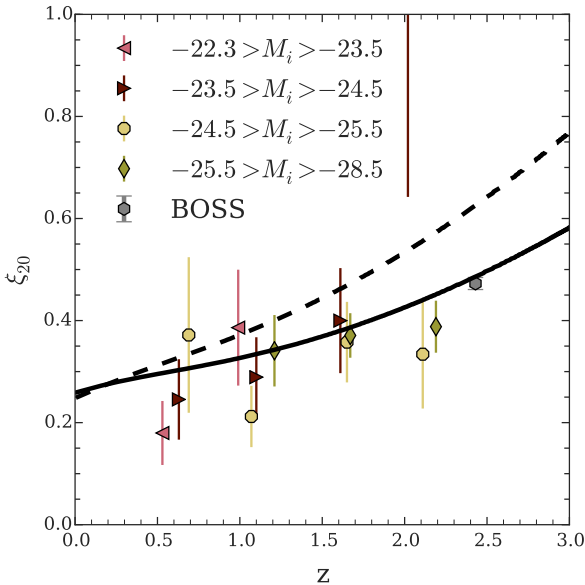


Figure 13. We show the measured ξ_{20}^Q for the bins from Section 6.3.2. We include model predictions for the evolution with redshift of ξ_{20}^Q . The solid line shows the expected $\xi_{20}^Q(z)$ relation assuming the empirical $b(z)$ relationship from equation 12. For comparison we show the empirical $b(z)$ relation from C05 as a dashed line, i.e. equation 4.

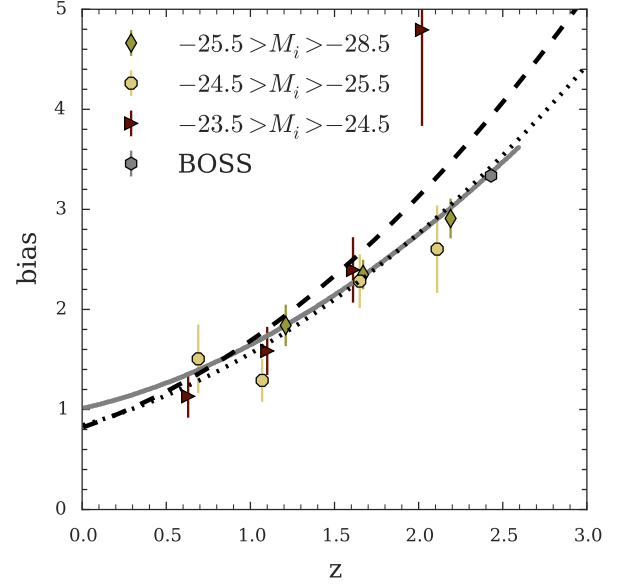


Figure 14. We show our estimate of quasar bias as a function of z and absolute magnitude. We include our measurement of bias from the BOSS survey, Eftekharzadeh et al. (2015). We show the evolution for a halo of mass $2 \times 10^{12} h^{-1} M_{\odot}$ as the solid grey line. We see that our measurements of bias are consistent with quasars inhabiting the same mass halos irrespective of magnitude or redshift. We include the 2QZ bias result (Equation 4) as a black dashed line and our bias result (Equation 12) as a dotted black line for comparison.

As such, our best-fit halo mass is lower than that of C05 but remains consistent at the 1σ level.

6.5 Comparison to XMM-COSMOS quasar clustering

The semi-analytic model presented by Fanidakis et al. (2013) predict that X-ray selected quasars inhabit higher mass halos than optically selected quasars. Fanidakis et al. (2013) present halo mass estimates from Allevato et al. (2011) and Krumpel et al. (2012) are presented as observational support to this model as these halo masses are higher ($\sim 10^{13} M_{\odot}$) than estimates from wide area optical studies ($\sim 10^{12} M_{\odot}$). In this section we briefly examine to whether this difference in halo mass estimates may be reconciled with the lack of dependence on optical luminosity found here. In particular, differences may occur due to differing analysis methods, and so we apply our method used for our optically selected samples to the X-ray selected sample of Allevato et al. (2011).

Allevato et al. (2011) measured the correlation function for quasars in the XMM-COSMOS field (Brusa et al. 2010) and found a clustering scale of $r_0 = 7.08^{+0.30}_{-0.28} h^{-1}$ Mpc and $\gamma = 1.88^{+0.04}_{-0.06}$. We examine the sample of quasars used in their work and that find $g_{\text{median}} = 21.4$ (~ 0.1 magnitudes fainter than the 2SLAQ sample) and their space density of quasars is $\sim 90 \text{ deg}^{-2}$ which is similar to that reached by 2QDESp, see Table A. Further, the redshift distribution of their X-ray selected sources (Figure 2; Allevato et al. 2011) is comparable to those of optically selected studies (see Figure 2). As we find no evidence for r_0 increasing with fainter magnitude, we believe their contradictory result worthy of further scrutiny.

Firstly, we note that an earlier clustering analysis of the

XMM-COSMOS quasars ($\sim 10\%$ fewer quasars than Allevato et al. 2011) was performed by Gilli et al. (2009) who measured $r_0 = 7.03^{+0.96}_{-0.89} h^{-1} \text{ Mpc}$ with $\gamma=1.8$. We use the R.A.–Dec. mixing approach of Gilli et al. (2009) to generate a random catalogue. However, instead of measuring $w(r_p)$ we measure the redshift correlation function, $\xi(s)$, for these data, assuming $\gamma = 1.8$ as in Section 6.3.1 for the fit. Gilli et al. (2009) compared this method of random generation to modelling the angular distribution and found that it can underestimate the true correlation length. Applying the correction from Gilli et al. (2009) we find that the amplitude of clustering is described by $r_0 = 6.03^{+0.80}_{-1.00} h^{-1} \text{ Mpc}$. This is in agreement with the measurements of quasar clustering at $z \approx 1.5$ found in this work.

Both the r_0 measurements from Gilli et al. (2009) and Allevato et al. (2011) use the projected correlation function, $w(r_p)$, as opposed to the redshift-space correlation function, $\xi(s)$, that we use. By remeasuring the correlation function we are able to compare directly to optical results. As noted by other authors (Mountrichas & Georgakakis 2012; Krumpel et al. 2012) this approach should provide a more robust comparison than comparing between different bias or halo mass models.

We also note that our errors (and those of Gilli et al. 2009) assume Poisson statistics and still lead to a factor of $2\text{--}3\times$ larger errors on r_0 than the $\approx \pm 0.3 h^{-1} \text{ Mpc}$ quoted by Allevato et al. (2011); it is not clear why this is the case. If the statistical errors on the XMM-COSMOS results are as large as found by Gilli et al. (2009) and ourselves then we conclude that these data contain no significant evidence for luminosity dependent clustering e.g. compared to their brighter counterparts in Figure 9 (see also discussion in next section).

6.6 Baryonic Acoustic Oscillations

Here we extend our analysis of the combined quasar sample to larger scales. In Figure 15 we show the result of combining the four correlation functions from each of the four surveys, weighting inversely according to the square of the errors at each separation (section 6.3.1). We measure $r_0 = 6.10 \pm 0.15 h^{-1} \text{ Mpc}$ for a sample containing 70940 quasars with $\langle z \rangle = 1.49$. Combining these surveys gives an effective volume of $\approx 0.6 h^{-3} \text{ Gpc}^3$, larger than the original SDSS LRG survey of Eisenstein et al. (2005) ($\approx 0.55 h^{-3} \text{ Gpc}^3$) or the 2dFGRS survey of Cole et al. (2005) ($\approx 0.1 h^{-3} \text{ Gpc}^3$) where BAO were detected. We use CAMB to predict the ΛCDM correlation function and scale this model to agree with the measured $\xi(s)$ at intermediate scales, $5 < s < 55 h^{-1} \text{ Mpc}$ (see Figure 15). Comparing the model to the data $\xi(s)$ at larger scales, $60 < s < 200 h^{-1} \text{ Mpc}$, we find that the model with the BAO feature is fit with $\chi^2, \text{df.} = 5.5, 4$ and $p\text{-value} = 0.23$ compared to $\chi^2, \text{df.} = 6.1, 4$ and $p\text{-value} = 0.19$ for a similar model without BAO. Although the model with the BAO feature fits better, the reduction in χ^2 is not significant ($\Delta\chi^2 \approx 0.6$) and so it is not possible to claim that the BAO feature is detected in this combined quasar survey.

We consider possible explanations for this lack of detection. Firstly, the statistical errors are still relatively large, larger still once the off-diagonal covariance matrix elements are considered, motivating the need for bigger samples with larger effective volumes at the BAO scale. However, we have argued above that the effective volume should already be large enough for the detection of this feature. Secondly, it does not appear that the $\pm 750 \text{ km s}^{-1}$ quasar redshift error plus intrinsic velocity dispersion affect the detectability of the BAO peak, as evidenced by convolving the ΛCDM model with Gaussians of this width. Our 9% fraction of misidentified quasar redshifts will reduce the BAO signal and the small scale

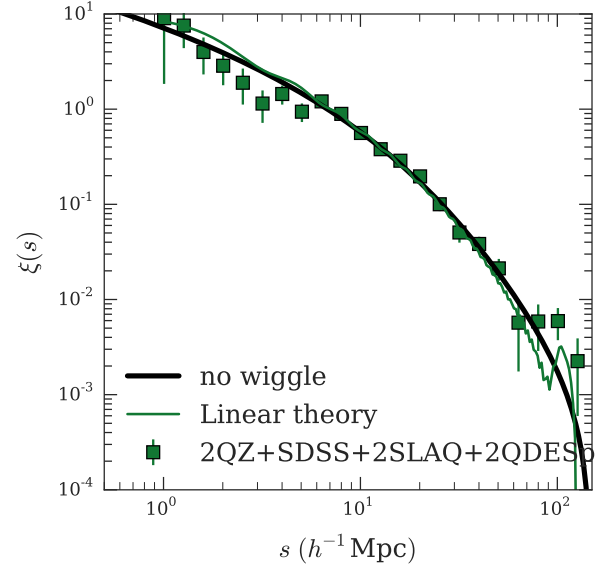


Figure 15. At each s bin we combine the values of the correlation function $\xi(s)$ for each of the four surveys using the error weighted mean. This combined sample consists of $N_{QSO} = 70\,940$ with mean redshift $\bar{z} = 1.49$. We fit our model form Section 6.1.2 to the data and find a best-fit value for $r_0 = 6.10 \pm 0.10 h^{-1} \text{ Mpc}$ with $\chi^2, \text{df.} = 15.6, 10$ where we fit in the range $5 < s (h^{-1} \text{ Mpc}) < 55$ (shown as the solid line). We also include the prediction of linear theory from CAMB and the ‘no wiggle’ model of Eisenstein & Hu (1998) with both normalised to our correlation function amplitude between $5 < s (h^{-1} \text{ Mpc}) < 55$.

signal in proportion and so this effect has already been accounted for in Figure 15 by our procedure of scaling the model to the observed small-scale $\xi(s)$. Thus it remains unclear why the BAO peak is undetected in these data.

7 DISCUSSION

We have analysed quasar clustering using surveys covering a wide range of fluxes and luminosities. We have found that there is little evidence for an increase of clustering amplitude with luminosity within the optical surveys at fixed redshift. Even including the XMM-COSMOS survey, we still find no evidence for the dependence of the clustering scale on luminosity. Following S11 we assume a halo-black hole mass relation of the form $M_{BH} \sim M_{Halo}^{1.82}$ (Ferrarese 2002) and the bias $b \sim M_{Halo}^{0.2}$ (Martini & Weinberg 2001) together with a fixed Eddington ratio we expect the approximate relation $r_0 \propto b \propto M_{BH}^{0.1} \propto L^{0.1}$. Given the factor of ≈ 10 increase in luminosity between the SDSS and 2SLAQ samples, a factor of ≈ 1.25 increase in r_0 is predicted, corresponding to r_0 increasing from 6.20 (2SLAQ) to $7.75 h^{-1} \text{ Mpc}$, significantly ($\approx 4\sigma$) higher than the observed value from SDSS. Thus, the observed luminosity dependence of the clustering amplitude is about a fifth of what is predicted on the basis of this simple model. This is confirmed by the formal χ^2 fits of the $L^{0.1}$ model in Figure 9. Excluding XMM-COSMOS, we find $\chi^2, \text{df.} = 7.8, 3$ and $p\text{-value} = 0.05$ for the $L^{0.1}$ model compared to $\chi^2, \text{df.} = 3.8, 3$ and $p\text{-value} = 0.23$ for the L -independent case. Including XMM-COSMOS, the same preference for the L independent model is shown, although the $L^{0.1}$

model is slightly less rejected with p -value=0.10. But if the XMM-COSMOS r_0 was closer to its corrected value of $r_0=6.0 h^{-1}\text{Mpc}$, rather than the $r_0=5.2 h^{-1}\text{Mpc}$ we have assumed here, then the level of rejection of the $L^{0.1}$ model would again be increased. We conclude that any dependence of clustering amplitude with luminosity is smaller than expected from a simple halo model.

When we then sub-divided the combined SDSS, 2QZ, 2SLAQ and 2QDESp surveys by absolute magnitude and redshift to increase the dynamic range in luminosity, we again found no evidence for luminosity dependent clustering at fixed redshift. However, we note that we do have significant evidence for the dependence of r_0 on redshift. We introduced a new bias model for $b(z)$ (equation 4), superseding that of C05. We find that our model for the evolution of bias with redshift is consistent with the higher $r_0 = 7.25 \pm 0.10 h^{-1}\text{Mpc}$ measured by Eftekharzadeh et al. (2015) in the BOSS quasar survey at $z \approx 2.4$.

The 2QZ results of C05 suggest that a fixed halo mass of $\sim 10^{12.5} M_\odot$ fits the z dependence of quasar clustering. Here we have confirmed the results of S11 that at approximately fixed redshift the clustering amplitude is approximately constant with luminosity. The apparent luminosity independence would suggest that the halo mass and hence black hole mass was virtually constant as a function of both luminosity and redshift.

If all quasars have the same black hole mass over a wide range of luminosity then there is a contradiction with all quasars radiating at a fixed fraction of Eddington as suggested from reverberation studies of nearby quasars (Peterson et al. 2004). To reconcile these two observations requires that the BH–halo mass relation is broken. There is some evidence for this from the work of Kormendy & Bender (2011) who found that the BH mass was more related to bulge mass than halo mass. In this view quasars would find themselves in similar sized haloes but with black hole masses more related to their luminosity.

A weak clustering dependence on luminosity is expected in ‘flickering’ models where the duty cycle for AGN activity is short and the quasar luminosity is highly variable (Lidz et al. 2006). The luminosity of a quasar may also be taken as implying a lower limit to its black-hole mass via the Eddington limit. Thus low luminosity quasars must be accreting at a highly sub-Eddington rate if the halo-mass BH mass relation is to be preserved, since they have similar halo masses to their brighter counterparts. This means that quasars are preferentially seen in bright phases. S11 again noted that this model contradicts the established correlation from reverberation mapping between black hole mass and luminosity (Peterson et al. 2004) but otherwise fits the clustering data (by design).

In Section 6.4.1 we estimate the halo bias for optically selected quasars between $0.3 < z < 2.9$ and $-28.5 < M_{i(z=2)} < -23.5$. In agreement with earlier works (C05; dA08; R09; S11) we find a characteristic halo mass of $M_{\text{Halo}} = 2 \pm 1 \times 10^{12} h^{-1} M_\odot$. Recent measurements of quasar clustering from X-ray surveys (Gilli et al. 2009; Allevato et al. 2011; Krumpe et al. 2012) have estimated significantly higher halo masses ($\sim 10^{13} M_\odot$) than the above optically selected samples.

Semi-analytical models of AGN (Fanidakis et al. 2013) have suggested that this is a physical result caused by a difference in AGN fuelling modes between optically selected and X-ray selected samples. However, given the susceptibility of soft X-ray selection ($\approx 0.1 - 2 \text{ keV}$) to intrinsic obscuration we would expect these two selections to sample the same population of AGN. This is supported by the similar space density and redshift distribution of unobscured X-ray AGN and optically selected quasars (see Allevato et al. 2011).

Indeed, both Krumpe et al. (2012) and Allevato et al. (2011) explicitly compare the clustering of optically selected quasars with unobscured X-ray AGN in their two samples. In both papers these authors find that the clustering of both populations (at any redshift) may be described by the same halo mass. Contrary to the claim of Allevato et al. (2011) we find consistent clustering of X-ray and optically selected samples. As such, we see little evidence for the higher halo masses in these studies (c.f. optical studies) that would support the suggestion of Fanidakis et al. (2013) that the two populations are driven by different accretion modes. The analysis by Mountrichas et al. (2013) suggests that higher X-ray AGN masses are in fact driven by X-ray AGN from groups. After excluding these AGN, Mountrichas et al. (2013) find the clustering of X-ray selected AGN is described by a halo mass $5_{-3}^{+4} \times 10^{12} h^{-1} M_\odot$, consistent with the clustering results presented here.

Krumpe et al. (2012) discuss the impact of HOD vs. power-law models for estimating bias from the correlation function. We agree that this may contribute to the differences in halo mass estimates. We further note that the deepest X-ray samples come from small areas on the sky and suffer from poorer statistics and greater susceptibility to sample variance than the larger area optical studies. This discrepancy could be well addressed by a large sample of deep X-ray selected AGN. Ongoing surveys such as eBOSS and the upcoming eROSITA survey have the opportunity to provide a homogeneous dataset of quasars up to $z \lesssim 2.2$. This may allow us to determine which physical processes drive accretion at different redshifts and how these processes interact to result in quasar clustering appearing largely independent of optical luminosity.

8 CONCLUSIONS

We have characterised a new quasar selection for quasars at intermediate redshifts $0.8 \leq z \leq 2.5$ and we demonstrate that the WISE All-Sky data release is complete for quasars in the redshift range (with $g < 20.5$). To account for photometric incompleteness for quasars fainter than this limit, to $g \approx 22.5$, requires traditional optical selection methods.

The 2QDES pilot survey has shown that a high density quasar survey is viable with the photometry from VST ATLAS and WISE. In fact the 2QDESp survey with 4% of the area of SDSS has 20% more effective volume to detect the BAO peak due to its $\approx 8\times$ higher quasar density. But even with 10000 quasars from 2QDESp combined with those from SDSS, 2QZ and 2SLAQ, we still lack a large enough effective volume to measure the BAO peak in the two-point correlation function although we gain some advantage in the precision of the clustering scale length, r_0 .

Direct comparison between the quasar correlation functions of SDSS, 2QZ, 2QDESp and 2SLAQ surveys, that range over an order of magnitude in quasar luminosity, show the same hint of higher r_0 at higher (SDSS) luminosities that was seen by Shen et al. (2009) and S11. However, the errors are such that a luminosity independent r_0 cannot be rejected by these data.

We combine the clustering measurements from 2QZ, 2SLAQ, SDSS and 2QDESp in the $M - z$ plane to search further for luminosity and redshift dependence. Contrary to the above hint, we find some tentative evidence here that *fainter* quasars may be more *strongly* clustered than brighter quasars at fixed (high) redshift ($z > 1.5$), albeit weakly detected. But overall the results remain consistent with a fixed quasar r_0 at fixed redshift, independent of luminosity.

We measure a significant redshift dependence of quasar clus-

tering and see that this dependence explains the higher r_0 measurements from Eftekharzadeh et al. (2015). Comparison of the redshift dependence of quasar clustering to the halo model shows that our data (and that of Eftekharzadeh et al. (2015)) is consistent with quasars inhabiting $2 \times 10^{12} M_\odot$ halos irrespective of redshift or quasar luminosity. These results are usually explained by a ‘flickering’ quasar model with a short duty cycle where quasars over a wide range of luminosities have similar halo, and hence black hole, masses. However, such models are inconsistent with the strong correlation between black hole and luminosity found from reverberation mapping. Shanks et al. (2011) indicated that the quasar clustering and reverberation mapping results might only be reconciled by breaking the black hole mass-halo mass correlation, as suggested by Kormendy & Bender (2011).

We also found similar clustering scale lengths ($r_0 \approx 6 h^{-1} \text{Mpc}$ for quasars in the XMM-COSMOS field, with little evidence that such quasars show a higher clustering amplitude than their more luminous, optically selected counterparts, as previously reported. This means that there is less evidence for higher halo masses at low redshift for AGN accreting in the hot halo mode, as suggested by Fanidakis et al. (2013).

9 ACKNOWLEDGMENTS

The VST-ATLAS survey is based on observations made with ESO telescopes at the La Silla Paranal Observatory under programme ID 177.A-3011. We are indebted to the CASU for reducing the ATLAS images and producing catalogues. This publication makes use of data products from the Wide-field Infrared Survey Explorer, which is a joint project of the University of California, Los Angeles, and the Jet Propulsion Laboratory/California Institute of Technology, funded by the National Aeronautics and Space Administration. The 2QDES pilot survey was based on observations made with the AAT and we would like to thank the staff of the Australian Astronomical Observatory for their contribution to this work. We thank Nicholas Ross for useful discussions on the quasar selection and the anonymous referee for improving the quality of this manuscript. This work makes use of the `runz` redshifting code developed by Will Sutherland, Will Saunders, Russell Cannon and Scott Croom. BC, TS, SF and DP are incredibly grateful for the efforts of the NSW Rural Fire Service who worked to ensure our safe evacuation of the site during the 2013 bushfire. This work was supported by the Science and Technology Facilities Council [ST/K501979/1, ST/L00075X/1].

10 REFERENCES

REFERENCES

- Allevato V., et al., 2011, *The Astrophysical Journal*, 736, 99
 Bovy J., et al., 2011, *ApJ*, 729, 141
 Brusa M., Civano F., Comastri A., Miyaji T., 2010, *ApJ*, 716, 348
 Carnall A. C., et al., 2015, *MNRAS*, 451, L16
 Challinor A., Lewis A., 2011, *Phys. Rev. D*, 84, 043516
 Cole S., Percival W. J., Peacock J. A., Norberg P., Baugh C. M., 2005, *MNRAS*, 362, 505
 Croom S. M., Smith R. J., Boyle B. J., Shanks T., Miller L., Outram P. J., Loaring N. S., 2004, *MNRAS*, 349, 1397
 Croom S. M., et al., 2005, *MNRAS*, 356, 415
 Croom S. M., Richards G. T., Shanks T., 2009, *Monthly Notices of the Royal Astronomical Society*, 392, 19
 Debes J. H., Hoard D. W., Wachter S., Leisawitz D. T., Cohen M., 2011, *The Astrophysical Journal Supplement Series*, 197, 38
 Eftekharzadeh S., et al., 2015, *MNRAS*, 453, 2779
 Eisenstein D. J., Hu W., 1998, *ApJ*, 496, 605
 Eisenstein D. J., Zehavi I., Hogg D. W., Scoccimarro 2005, *ApJ*, 633, 560
 Fanidakis N., et al., 2013, *MNRAS*, 435, 679
 Ferrarese L., 2002, *ApJ*, 578, 90
 Fine S., et al., 2006, *MNRAS*, 373, 613
 Fine S., et al., 2012, *MNRAS*, 427, 2701
 Gilli R., Zamorani G., Miyaji T., 2009, *A&A*, 494, 33
 González-Solares E. A., Walton N. A., Greimel R., 2008, *MNRAS*, 388, 89
 Kaiser N., 1987, *MNRAS*, 227, 1
 Kirkpatrick J. a., Schlegel D. J., Ross N. P., Myers A. D., Hennawi J. F., Sheldon E. S., Schneider D. P., Weaver B. a., 2011, *The Astrophysical Journal*, 743, 125
 Kormendy J., Bender R., 2011, *Nature*, 469, 377
 Krumpke M., Miyaji T., Coil A. L., Aceves H., 2012, *ApJ*, 746, 1
 Kuijken K., Bender R., Cappellaro E., 2004, *J 10.1117/12.550892*, 5492, 484
 Landy S. D., Szalay A. S., 1993, *ApJ*, 412, 64
 Lewis A., Challinor A., Lasenby A., 2000, *ApJ*, 538, 473
 Lidz A., Hopkins P. F., Cox T. J., Hernquist L., Robertson B., 2006, *ApJ*, 641, 41
 Maddox N., Hewett P. C., Péroux C., Nestor D. B., Wisotzki L., 2012, *MNRAS*, 424, 2876
 Martini P., Weinberg D. H., 2001, *ApJ*, 547, 12
 McMahon R. G., Banerji M., Gonzalez E., Koposov S. E., Bejar V. J., Lodieu N., Rebolo R., VHS Collaboration 2013, *The Messenger*, 154, 35
 Mo H. J., White S. D. M., 1996, *MNRAS*, 282, 347
 Mountrichas G., Georgakakis A., 2012, *MNRAS*, 420, 514
 Mountrichas G., et al., 2013, *MNRAS*, 430, 661
 Navarro J. F., Frenk C. S., White S. D. M., 1997, *ApJ*, 490, 493
 Palanque-Delabrouille N., Magneville C., Yèche C., 2013, *A&A*, 551, A29
 Peebles P. J. E., 1980, *The large-scale structure of the universe*
 Peterson B. M., Ferrarese L., Gilbert K. M., 2004, *ApJ*, 613, 682
 Planck Collaboration Ade P. A. R., Aghanim N., 2014, *A&A*, 571, A16
 Ratcliffe A., 1996, PhD thesis, PhD thesis, Univ. of Durham, (1996)
 Richards G. T., Fan X., Newberg H. J., 2002, *AJ*, 123, 2945
 Richards G. T., Nichol R. C., Gray A. G., 2004, *ApJS*, 155, 257
 Richards G. T., Croom S. M., Anderson S. F., 2005, *MNRAS*, 360, 839
 Richards G. T., Strauss M. A., Fan X., 2006, *AJ*, 131, 2766
 Ross N. P., et al., 2009, *The Astrophysical Journal*, 697, 1634
 Saunders W., Cannon R., Sutherland W., 2004, *Anglo-Australian Observatory Epping Newsletter*, 106, 16
 Schlegel D. J., Finkbeiner D. P., Davis M., 1998, *ApJ*, 500, 525
 Schneider D. P., Hall P. B., Richards G. T., 2007, *AJ*, 134, 102
 Seljak U., Zaldarriaga M., 1996, *ApJ*, 469, 437
 Shanks T., Croom S. M., Fine S., Ross N. P., Sawangwit U., 2011, *MNRAS*, 416, 650
 Shanks T., et al., 2015, *MNRAS*, 451, 4238
 Shen Y., et al., 2009, *The Astrophysical Journal*, 697, 1656
 Sheth R. K., Mo H. J., Tormen G., 2001, *MNRAS*, 323, 1
 Smith R. J., Croom S. M., Boyle B. J., Shanks T., Miller L., Loaring N. S., 2005, *MNRAS*, 359, 57
 Taylor M. B., 2005, in Shopbell P., Britton M., Ebert R., eds, *Astronomical Society of the Pacific Conference Series Vol. 347, Astronomical Data Analysis Software and Systems XIV*, p. 29
 Taylor M. B., 2006, in Gabriel C., Arviset C., Ponz D., Enrique S., eds, *Astronomical Society of the Pacific Conference Series Vol. 351, Astronomical Data Analysis Software and Systems XV*, p. 666
 Wright E. L., Eisenhardt P. R. M., Mainzer A. K., 2010, *AJ*, 140, 1868
 Zaldarriaga M., Seljak U., 2000, *ApJS*, 129, 431
 da Ângela J., Outram P. J., Shanks T., Boyle B. J., Croom S. M., Loaring N. S., Miller L., Smith R. J., 2005, *MNRAS*, 360, 1040
 da Ângela J., et al., 2008, *MNRAS*, 383, 565
 de Jong J. T. A., Kuijken K., Applegate D., 2013, *The Messenger*, 154, 44

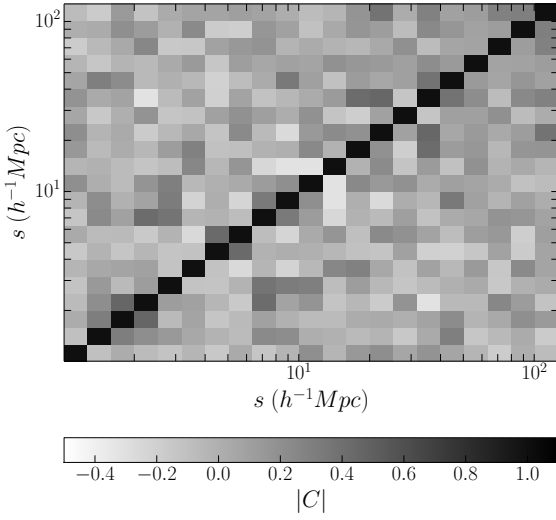


Figure B1. The normalised covariance matrix (see Equation B2) for $\xi(s)$ with jackknife errors calculated from dividing our sample into the separate 2dF pointings.

APPENDIX A: DETAILS OF OBSERVATIONS

APPENDIX B: COVARIANCE MATRIX

We calculate the covariance matrix for our full sample, described in Section 5.2. Using a similar approach of R09, we calculate the inverse-variance weighted covariance matrix, C_{ij} by

$$C_{ij} = \sum_{L=1}^N \sqrt{\frac{DR_L(s_i)}{DR(s_i)}} [\xi_L(s_i) - \xi_{total}(s_i)] \times \sqrt{\frac{DR_L(s_j)}{DR(s_j)}} [\xi_L(s_j) - \xi_{total}(s_j)] \quad (\text{B1})$$

where DR denotes the number of quasar-random pairs remaining when we *exclude* subregion L from the analysis. We recalculate ξ_L (see Equation 2) for the remaining sample, after excluding the specified region, L . In Figure B1 we present the covariance matrix for our sample. We normalise the matrix such that

$$|C| = \frac{C_{ij}}{\sigma_i \sigma_j} \quad (\text{B2})$$

APPENDIX C: OBSERVATION POINTINGS

Field	Date	N_{Stars}	N_Q	$N_Q \leq 20.5$	$\frac{S}{N}$	QSO_{lim}	u_{lim}	Algorithm	Repeat	Comment
hh:mm:ss:mm		deg ⁻²	deg ⁻²	deg ⁻²		[AB]	[AB]			
0231–3002 2011:12:20		1881	64.33	28.03	2.55	21.72	22.13	<i>ugriXDQSO</i>	0	
1046–0704 2012:04:28		3122	26.11	14.65	1.25	21.14	21.93	<i>ugriXDQSO</i>	0	
1236–0704 2012:04:28		3427	37.90	20.06	2.76	21.21	22.13	<i>ugriXDQSO</i>	0	
1301–0704 2012:04:28		3569	46.50	20.38	2.29	21.48	22.16	<i>ugriXDQSO</i>	0	
1004–0704 2012:04:28		3595	47.13	19.11	3.00	21.50	22.01	<i>ugriXDQSO</i>	0	
1444–0704 2012:04:28		5422	27.39	15.61	0.93	21.72	22.10	<i>ugriXDQSO</i>	0	
2122+0000 2012:04:28		8850	39.17	17.20	0.96	21.99	21.87†	<i>ugriXDQSO</i>	0	
1219–0704 2012:04:29		3346	49.36	23.89	2.38	21.57	22.02	<i>ugriXDQSO</i>	0	
1244–0704 2012:04:29		3483	45.22	22.29	2.27	21.37	22.22	<i>ugriXDQSO</i>	0	
1309–0704 2012:04:29		3563	50.32	19.75	2.48	21.51	22.10	<i>ugriXDQSO</i>	0	
1453–0704 2012:04:29		5451	37.90	23.25	2.29	21.52	22.05	<i>ugriXDQSO</i>	0	
0300+0000 2012:11:04		2221	45.22	22.29	1.65	22.07	21.87†	<i>ugriXDQSO</i>	0	
2342–3102 2012:11:04		2412	61.47	24.52	4.68	21.55	22.11	<i>ugriXDQSO</i>	0	
2251–3102 2012:11:04		3200	60.19	22.61	3.74	21.57	22.08	<i>ugriXDQSO</i>	0	
0346–2604 2013:01:11		2264	71.97	24.20	4.48	21.88	22.04	<i>ugriXDQSO</i> W1W2	0	
0356–2903 2013:01:11		2458	72.61	34.08	4.29	21.77	22.02	<i>ugriXDQSO</i> W1W2	0	
1023–0903 2013:01:11		3668	50.64	21.97	4.97	21.76	21.81	<i>ugriXDQSO</i> W1W2	0	Twilight
1004–0803 2013:01:11		3771	59.55	21.34	3.48	21.61	21.92	<i>ugriXDQSO</i> W1W2	0	
0356–2604 2013:01:12		2320	64.65	29.62	2.50	21.73	22.08	<i>ugriXDQSO</i> W1W2	0	
1055–0903 2013:01:12		3478	55.10	23.57	2.66	21.66	21.88	<i>ugriXDQSO</i> W1W2	0	Twilight
1016–0903 2013:01:12		3818	50.00	25.48	2.93	21.62	21.83	<i>ugriXDQSO</i> W1W2	0	
0352–2804 2013:02:16		2518	67.52	30.57	2.78	21.62	21.88	<i>ugriXDQSO</i> W1W2	0	Moon
1029–0706 2013:02:16		3192	50.32	25.16	2.47	21.38	22.00	<i>ugriXDQSO</i> W1W2	0	
1218–0704 2013:02:16		3336	52.23	29.94	2.61	21.42	22.01	<i>ugriXDQSO</i> W1W2	0	
1227–0704 2013:02:16		3363	58.92	30.89	2.45	21.51	22.07	<i>ugriXDQSO</i> W1W2	0	
1021–0706 2013:02:16		3435	50.00	23.57	2.26	21.59	22.00	<i>ugriXDQSO</i> W1W2	0	
1012–0706 2013:02:16		3454	59.24	31.21	3.16	21.68	22.02	<i>ugriXDQSO</i> W1W2	0	
0330–3002 2013:02:17		2176	73.25	32.17	3.47	22.04	22.04	<i>ugriXDQSO</i> W1W2	0	Moon
1038–0706 2013:02:17		2931	57.64	25.48	2.97	21.63	21.98	<i>ugriXDQSO</i> W1W2	0	Moon
1046–0706 2013:02:17		3148	68.79	35.67	3.64	21.49	21.92	<i>ugriXDQSO</i> W1W2	0	
1055–0706 2013:02:17		3219	60.19	30.25	2.83	21.47	21.94	<i>ugriXDQSO</i> W1W2	0	
1235–0704 2013:02:17		3432	50.32	25.48	3.24	21.81	22.13	<i>ugriXDQSO</i> W1W2	0	
1252–0704 2013:02:17		3525	55.10	24.20	2.75	21.62	22.32	<i>ugriXDQSO</i> W1W2	0	
1318–0704 2013:02:17		3642	64.01	30.89	2.51	21.68	22.23	<i>ugriXDQSO</i> W1W2	0	
0339–3002 2013:02:18		2295	59.87	34.39	3.88	21.58	22.17	<i>ugriXDQSO</i> W1W2	0	Moon + Artefact
1046–0906 2013:02:18		3336	51.59	23.89	2.89	21.84	21.85	<i>ugriXDQSO</i> W1W2	0	Artefact
1038–0906 2013:02:18		3572	48.09	28.66	3.03	21.88	21.90	<i>ugriXDQSO</i> W1W2	0	Moon + Artefact
1434–0704 2013:02:18		5158	50.00	21.02	2.83	21.61	22.09	<i>ugriXDQSO</i> W1W2	0	Artefact
1442–0704 2013:02:18		5408	49.36	21.97	2.92	21.82	22.10	<i>ugriXDQSO</i> W1W2	0	Artefact
1508–0704 2013:02:18		6623	49.68	22.61	3.25	21.67	22.07	<i>ugriXDQSO</i> W1W2	0	Artefact
0349–3002 2013:02:19		2392	59.87	33.44	5.74	21.68	22.13	<i>ugriXDQSO</i> W1W2	0	Moon + Artefact
1103–0906 2013:02:19		3253	54.46	23.89	4.14	21.85	21.86	<i>ugriXDQSO</i> W1W2	0	Moon + Artefact
1103–0905 2013:02:19		3275	23.25	10.83	3.32	21.85	21.86	<i>ugriXDQSO</i> W1W2	0	Artefact, repeated in error
1451–0704 2013:02:19		5344	59.55	27.07	3.18	21.63	22.05	<i>ugriXDQSO</i> W1W2	0	Artefact
1459–0704 2013:02:19		6186	33.44	13.38	3.25	21.82	22.06	<i>ugriXDQSO</i>	0	Artefact
1516–0704 2013:02:19		7287	45.22	19.11	2.59	21.63	22.05	<i>ugriXDQSO</i> W1W2	0	Twilight + Artefact
2307–2601 2013:07:28		2981	9.87	2.23	1.17	21.60	22.07	<i>ugriXDQSO</i> W1W2	1	
2307–2601 2013:07:28		2982	55.10	26.75	2.35	21.60	22.07	<i>ugriXDQSO</i> W1W2	0	
1442–1500 2013:07:28		6865	57.01	19.75	2.41	21.93	21.80	<i>ugriXDQSO</i> W1W2	0	
1442–1500 2013:07:28		6868	11.78	1.91	1.67	21.93	21.80	<i>ugriXDQSO</i> W1W2	1	
1500–1500 2013:07:28		7987	52.23	24.20	3.05	21.75	21.96	<i>ugriXDQSO</i> W1W2	0	
1500–1500 2013:07:28		7990	8.60	1.59	1.92	21.75	21.96	<i>ugriXDQSO</i> W1W2	1	
2316–2601 2013:07:29		2957	69.11	33.76	2.63	21.75	22.16	<i>ugriXDQSO</i> W1W2	0	Cloud in Field
2133–2807 2013:07:29		5579	17.52	2.23	1.63	21.69	21.98	<i>ugriXDQSO</i> W1W2	1	Cloud in Field
2133–2807 2013:07:29		5581	45.54	26.11	1.66	21.69	21.98	<i>ugriXDQSO</i> W1W2	0	Cloud in Field
1451–1500 2013:07:29		7389	44.90	23.57	6.32	21.79	21.86	<i>ugriXDQSO</i> W1W2	0	
1451–1500 2013:07:29		7390	13.38	1.91	2.32	21.75	21.86	<i>ugriXDQSO</i> W1W2	1	
1508–1500 2013:07:29		8390	38.53	15.29	1.57	21.78	21.93	<i>ugriXDQSO</i> W1W2	0	Cloud in Field
2258–2807 2013:07:30		2962	19.43	2.23	2.11	21.72	21.91	<i>ugriXDQSO</i> W1W2	1	
2258–2807 2013:07:30		2964	60.19	30.25	2.03	21.84	21.91	<i>ugriXDQSO</i> W1W2	0	
2133–2601 2013:07:30		5443	16.24	1.59	1.59	21.69	22.06	<i>ugriXDQSO</i> W1W2	1	
2133–2601 2013:07:30		5443	66.56	28.98	3.02	21.69	22.06	<i>ugriXDQSO</i> W1W2	0	
1508–1500 2013:07:30		8391	19.11	2.55	1.57	21.89	21.93	<i>ugriXDQSO</i> W1W2	1	
1526–1500 2013:07:30		9992	49.36	19.75	2.32	21.78	21.79	<i>ugriXDQSO</i> W1W2	0	
2316–2601 2013:07:31		2957	21.97	4.14	1.49	21.75	22.16	<i>ugriXDQSO</i> W1W2	1	
2215+0014 2013:07:31		4426	50.00	20.06	3.08	21.84	21.87†	<i>ugriXDQSO</i> W1W2	0	

Field	Date	N_{Stars}	N_Q	$N_{Q \leq 20.5}$	$\frac{S}{N}$	QSO_{lim}	u_{lim}	Algorithm	Repeat	Comment
hh:mm±dd:mm		deg ⁻²	deg ⁻²	deg ⁻²		[AB]	[AB]			
2152–2601	2013:07:31	4899	61.78	28.98	2.40	21.79	22.06	<i>ugriXDQSOW1W2</i>	0	
2152–2601	2013:07:31	4901	15.92	0.96	1.36	21.79	22.06	<i>ugriXDQSOW1W2</i>	1	
1447–1858	2013:07:31	8648	5.41	1.59	1.87	21.72	21.91	<i>ugriXDQSOW1W2</i>	1	
1447–1858	2013:07:31	8650	53.82	20.38	3.81	21.72	21.91	<i>ugriXDQSOW1W2</i>	0	
1526–1500	2013:07:31	9993	7.64	2.23	1.53	21.78	21.79	<i>ugriXDQSOW1W2</i>	1	

Table A1. N_{Stars} are the number of point sources brighter than $g = 21.5$, N_Q is the number of spectroscopically confirmed quasars deg⁻² in that field, $\frac{S}{N}$ is the mean signal-to-noise per pixel. $N_{Q \leq 20.5}$ are the number of spectroscopically confirmed quasars deg⁻² in a field brighter than $g = 20.5$. QSO_{lim} is the limit in g that contains 90% of our quasar sample in that field. u_{lim} is the average 5σ limit in u for the stacked images that make up a 2dF field. The algorithm specifies whether we select quasars using the XDQSO algorithm and optical colour selection alone or whether we used WISE photometry as well. Repeated fields are fields that were observed for a second time with new fibre allocations. † 5σ u -band limits for SDSS imaging are the characteristic SDSS limits as shown in [Shanks et al. \(2015\)](#).

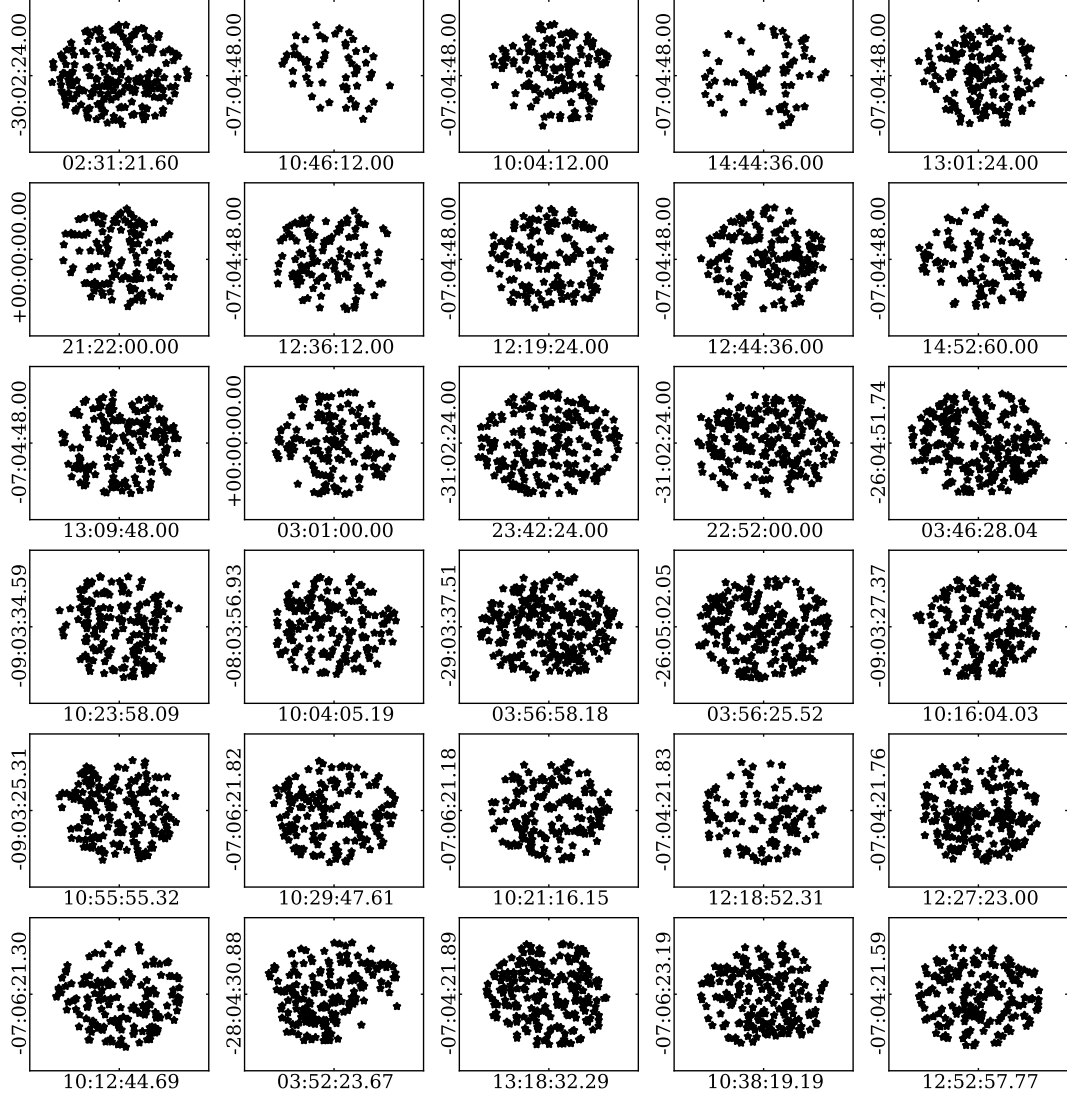
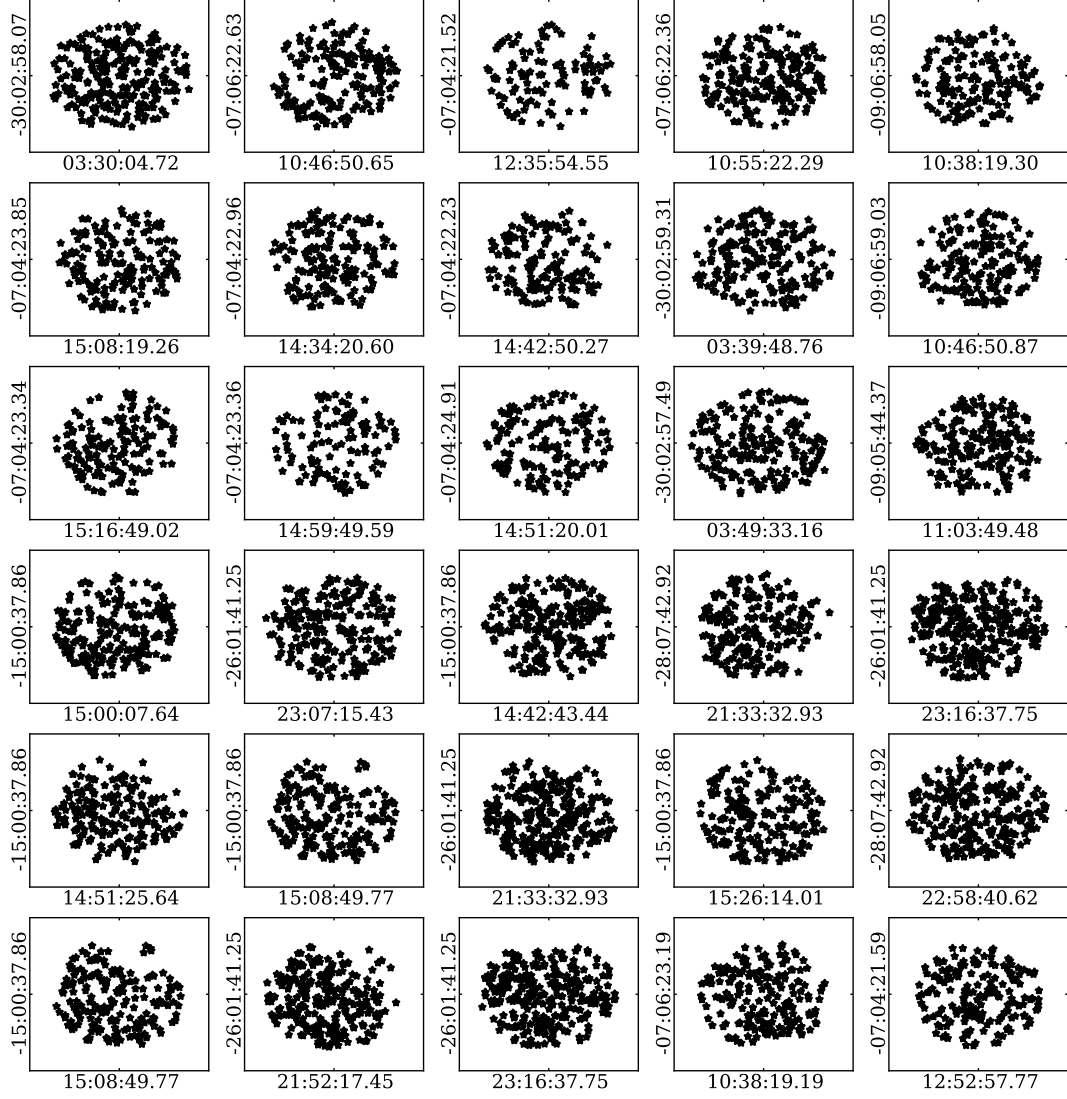


Figure C1. We show the quasar sample obtained from each 2dF pointing. The field at 11:03:49.48 – 09:05:44.37 was repeated in error. This provided us with duplicate redshifts for the same quasars. These were analysed to provide redshift error estimates found in Section 5.2.1.



This paper has been typeset from a \LaTeX file prepared by the author.